Nanoscale

PAPER

View Article Online
View Journal



Cite this: DOI: 10.1039/d5nr03192c

# Surfactant-templated syntheses of nanostructured high-entropy spinel oxide electrocatalysts and effects on water-splitting

Jimodo J. Ogada, Augustus K. Lebechi, Aderemi B. Haruna and Kenneth I. Ozoemena *

The production of clean and affordable hydrogen energy relies on the development of affordable, efficient, and durable bifunctional electrocatalysts for overall water-splitting. In this research, a quinary high-entropy inverse spinel oxide, $(CoCuFeMnNi)_3O_4$, was prepared *via* the reverse co-precipitation method, employing different surfactants as templates, namely, PVP, SDS, and CTAB. XRD, SEM, XPS, and HRTEM were employed to analyze the structure, morphology, and other properties of $(CoCuFeMnNi)_3O_4$. The effects of the different surfactants on the properties and electrocatalytic performance of $(CoCuFeMnNi)_3O_4$ in water-splitting reactions (HER/OER) were discussed. The results show that different surfactants influence the dispersion, surface area, and other properties of the synthesized $(CoCuFeMnNi)_3O_4$ particles. The electrochemical test results of the HER and OER were compared. Due to the superior performance of the PVP-assisted $(CoCuFeMnNi)_3O_4$ in the HER and OER, PVP was selected as the surfactant of choice. From the metal salt-to-PVP ratio studies, HESOx with 1 wt% PVP as a synthesis template ($HESOx_{PVP\ 1\%}$) exhibited the best performance of all, requiring an overpotential of 16 mV to reach 10 mA $cm^{-2}$ in HER and 381 mV to reach 10 mA $cm^{-2}$ in the OER. The effects of the presence and absence of Cu on the HER and OER are also investigated. Quaternary MESOx ($(CoFeMnNi)_3O_4$) is compared to HESOx. Cu is observed to increase the SSA and ECSA of HESOx, giving it superior initial HER/OER performance. However, it suffers active site losses due to the ready formation of cuprous oxide ($Cu_2O$), leading to sluggish electrocatalysis at higher overpotentials. In the two-electrode test, HESOx reaches 10 mA $cm^{-2}$ at an overpotential of *ca.* 0.267 V, compared to the 0.43 V required by (MESOx). However, MESOx shows a remarkably superior performance than HESOx, improving by 130 mV after 100 h of activity.

Received 28th July 2025,
Accepted 10th February 2026

DOI: 10.1039/d5nr03192c

rsc.li/nanoscale



## Introduction

The global energy crisis and environmental concerns have driven significant research into renewable energy sources. Among these, green hydrogen, produced through environment-friendly methods like water splitting, is a promising clean fuel. However, developing cost-effective electrocatalysts is imperative for enhancing the performance of water-splitting devices, particularly in alkaline medium. The oxygen evolution reaction (OER) and hydrogen evolution reaction (HER) are the two half-reactions involved in water splitting.

In alkaline media, the HER mechanism involves:

(i) Volmer/water dissociation:

$$H_2O + e^- + M \rightarrow H* + OH^-$$

Followed by the Heyrovsky or Tafel step

(ii) Heyrovsky step (desorption):

$$H* + H_2O + e^- \rightarrow H_2 + OH^- + M$$

or

(iii) Tafel step (combination):

$$2H* \rightarrow H_2$$

The Volmer, Heyrovsky, and Tafel steps have values of 118 mV $dec^{-1}$, 39 mV $dec^{-1}$, and 30 mV $dec^{-1}$, respectively. The Tafel slope is determined from the Tafel plot to identify the pathway and rate-determining step (RDS) of the HER.

The strength of metal–hydrogen (M–H) bonds can be used to predict the exchange current densities for HER across different electrocatalysts. Trasatti initially noted this pattern on metals in 1970.[1,2]

The OER mechanism in alkaline electrolyte involves the following steps:

(i) Hydroxide ion adsorption:

$$OH^-{}_{(aq)} + M \rightarrow OH*_{(ads)} + e^-$$

*Molecular Science Institute, School of Chemistry, University of the Witwatersrand, Johannesburg 2050, South Africa. E-mail: Kenneth.ozoemena@wits.ac.za*

(ii) Oxidation to hydroxyl radical:

$$H*_{(ads)} + OH^-_{(aq)} \rightarrow O*_{(ads)} + H_2O_{(l)} + e^-$$

(iii) Formation of hydroperoxyl radical:

$$O*_{(ads)} + OH^-_{(aq)} \rightarrow OOH*_{(ads)} + e^-$$

(iv) Oxygen evolution:

$$OOH*_{(ads)} + OH^-_{(aq)} \rightarrow M + O_{2(g)} + H_2O_{(l)} + e^-$$

where M represents the catalyst's active site, and the species adsorbed on these active sites are denoted as OH*, O*, and OOH*.[3] Other OER mechanisms are suggested in literature, such as lattice oxygen-mediated mechanism (LOM), which is particularly relevant in metal oxides, and involves the participation of lattice oxygen in the OER process, contributing to enhanced catalytic activity; and adsorbate evolution mechanism (AEM), involving the adsorption and subsequent reactions of various species on the catalyst surface.[4]

While the hydrogen ions in the electrolyte are reduced to form $H_2$ at the cathode, $OH^-$ oxidation occurs at the anode to form $O_2$.

The binding energy between the reaction intermediate and the catalyst's active site, and the water dissociation barrier determine the reaction kinetics of the HER and OER.[5–7] Theoretically, to initiate water-splitting under standard pressure and temperature (1 atm pressure and 25 °C), the minimum voltage required is 1.23 V. Nevertheless, practical water-splitting systems necessitate a potential higher than the theoretical to overcome the kinetic barriers at the electrodes due to various factors such as slow reaction kinetics, mass transport limitations, resistance within the system, and competing side reactions. The word "overpotential" ($\eta$) describes how much additional potential is required to achieve a specific current density. The smaller the overpotential ($\eta$) of an electrocatalyst is for the reaction of interest, the more superior the performance.[8,9]

Optimizing the performance of electrocatalysts for both reactions is essential for achieving high overall water-splitting. The low cost, availability, and outstanding electrochemical performance of high entropy alloys and their derivative oxides have made them an attractive choice for electrocatalysis.[10–15]

High entropy materials consist of a highly disordered arrangement of atoms, and due to this sort of arrangement, controlling their surface electronic structures and selectively exposing their active sites can be difficult.[16] These could potentially hamper their electrocatalytic activity. Researchers have tried different synthesis methods to fix these issues, but they are faced with shortcomings such as non-uniform particle shape and a wide range of particle size distribution. This is because, during the synthesis process, nanoparticles suffer a less stable colloidal system, which may result in the sorption of surrounding molecules to achieve stability, leading to the agglomeration/coagulation of the nanoparticles.[17] Many researchers have used surfactants as stabilizing agents to improve the stability of nanomaterials.[17–22]

Surfactants (also known as "surface active agents") are molecules that reduce the surface tension of liquids, allowing them to spread and mix more easily. In a solution in the water or oil phase, surfactants form micelles and absorb into the interface between that solution and another phase (solid or gaseous). Their ability to exhibit these two distinct properties is due to their chemical structures, which comprise two different functional groups with differing affinities within the same molecule.[23] These groups are simply referred to as the hydrophobic group (water-hating or oil-loving tail) and the hydrophilic group (water-loving head). Therefore, surfactants are usually described as being amphiphilic molecules (lovers of everything), making them versatile in various applications.

In an aqueous solution, the headgroup (hydrophilic side) of the molecule would break into anions, cations, or a combination of both (depending on the pH of the solution), while some do not dissociate into any ions (non-ionic). Therefore, surfactants are categorized into cationic, anionic, amphoteric, and non-ionic surfactants.[23,24] In nanomaterials synthesis, surfactants assist to:

(i) *Control the morphology of nanoparticles* – the shape and size of nanomaterials can be adjusted by adjusting the type and concentration of surfactants.

(ii) *Facilitate the dispersion of precursors* – surfactants ensure a uniform distribution of the precursor materials into the solution, thereby promoting the formation of well-defined structures.

(iii) *Stabilize the nanoparticles* – they form a protective layer around the particles. Thereby preventing agglomeration/coagulation of the particles.

The surfactant is chosen based on the specific nanomaterial and desired qualities. While surfactants are effective for dispersing nanomaterials in water, anionic and cationic surfactants might interact with precursor ions, thereby affecting the properties of the material. They may also be incompatible with certain precursors or solvents. Non-ionic surfactants, on the other hand, offer steric stabilization without introducing ionic charges, thereby minimizing interaction with precursors and leading to more consistent material properties. However, they may be less effective for charged nanomaterials compared to ionic surfactants and require careful selection for optimal compatibility. Ionic surfactants have better solubility than their non-ionic counterparts. However, non-ionic surfactants have the advantage of not changing the pH of the solution. In addition, their CMC (critical micelle concentration) is usually higher than those of ionic surfactants, allowing for the addition and mixing of more of the surfactant into the solution without concerns about the possible formation of undesired micelle.[25] Zwitterionic surfactants possess excellent stability as they possess both positive and negative charges within their structure, enabling effective stabilization of various nanomaterials in aqueous solutions. Zwitterionic charges can minimize unwanted interactions with precursors compared to ionic surfactants, leading to more consistent material properties. However, they can be more expensive compared to some ionic and non-ionic counterparts. In

 

addition to that, tailoring their structure for specific nanomaterials might require additional synthetic efforts.

Surfactant-assisted synthesis of catalyst materials has mainly been reported for different materials,[17,26–34] with only a few reports for high entropy materials.[35,36] In this research, $(CoCuFeMnNi)_3O_4$ high entropy oxide (HESOx) was prepared *via* co-precipitation, employing three different dispersants/surfactants, namely, polyvinylpyrrolidone (PVP, non-ionic), sodium dodecyl sulfate (SDS, anionic), and cetyltrimethylammonium bromide (CTAB, cationic), and using $NH_4OH$ as a precipitating agent. The selected elements are transition metals, which have nearly similar atomic radii to minimize local lattice distortion and promote the formation of a stable, single-phase, high-entropy material. Moreover, transition metals are known for their redox activities. Besides the size compatibility, the specific elements were chosen for their well-established electrocatalytic performance.[37,38] The synthesized materials (HESOx, HESOx-PVP, HESOx-SDS, and HESOx-CTAB) were characterized to study the effects of the different surfactants on the electronic modulation of HESOx. The samples were further tested as possible electrocatalysts for electrochemical water-splitting reactions.

## Experimental methods

### Synthesis of HESOx

The materials were synthesized using a simple reverse co-precipitation process.[39] To make an equimolar high-entropy oxide electrocatalyst, each metal precursor salt for Co, Cu, Fe, Mn, and Ni was weighed in equimolar ratios to a total of 16.0245 g and then stirred in 10 mL of water for 10 min, after which they were all stirred together in a 250 mL beaker for 30 min. 200 mL of 0.2 M ammonia solution ($NH_4OH$) was then added to the above solution and left to stir on the magnetic stirrer for 3 h at ambient temperature, followed by centrifugation and drying of the precipitate at 90 °C. The dried product was crushed and then calcined in air at 500 °C for 8 h with a ramp-up rate of 4 °C $min^{-1}$ and cooled to room temperature (HESOx yield: 1.523 g).

### Surfactant-aided synthesis of the HESOx

The same synthesis method was employed here. To make an equimolar high-entropy oxide electrocatalyst, each metal precursor salt for Co, Cu, Fe, Mn, and Ni was weighed in equimolar ratios to a total of 16.0245 g and then stirred in 10 mL of water for 10 min, after which they were all stirred together briefly in a 250 mL beaker. Three beakers of this solution were prepared. CTAB, SDS, and PVP were weighed to a metal salt–surfactant ratio of 1 : 0.005 (0.5 wt%) each and stirred in separate beakers in 10 mL ultrapure $H_2O$ until a fine solution was obtained. Each of the metal salt solutions prepared above was mixed with a surfactant solution and stirred for 30 min. 200 mL of 0.2 M ammonia solution ($NH_4OH$) was then added to each of the above solutions and allowed to stir on the magnetic stirrer for 3 hours at ambient temperature, followed by centrifugation and drying of the precipitate at 90 °C. This was followed by crushing in a mortar and calcination for 8 h in air at 500 °C at a heating rate of 4 °C $min^{-1}$ and finally cooling to room temperature. The obtained products were abbreviated as HESOx-CTAB, HESOx-SDS, and HESOx-PVP.

## Results and discussion

### Physicochemical characterizations

XRD (Fig. 1A) shows that the materials consist of a mixture of spinel and rock-salt phases. The peaks centered around 2$\theta$° values of 18.34°, 30.18°, 35.56°, 37.21°, 43.23°, 49°, 53.59°, 57.20°, and 62.74° are attributed to the reflections from the planes of (111), (220), (311), (222), (400), (321), (422), (511) and (440), and the high-intensity peak at (311), suggests an inverse spinel cubic structure.[40,41] The 2$\theta$° values are assigned to the reflections from the planes using the $Fe_3O_4$.

The properties (color, conductivity, diffusivity, catalytic performance, and magnetism) of spinel materials are influenced by the occupation of metals at their octahedral ($O_h$) and tetrahedral ($T_d$) sites. The distribution of the cations is influenced by the chemical environment and heat treatment process and can be characterized by the degree of inversion $x$, which adopts values between zero (for normal spinel materials) and 1 (inverse spinel materials) in the equation $(A_{1-x}B_x)_{tet}(A_xB_{2-x})_{oct}$.[42] Hence, while normal spinel have all the A-site (divalent) cations filling the $T_d$ sites and the B-site (trivalent) cations at the $O_h$ sites, an inverse spinel has its divalent cations occupying the $O_h$ sites while half of the trivalent cations fill the $T_d$ sites and the other half occupy the $O_h$ sites and can be represented as $B^{3+}[A^{2+}B^{3+}]O_4$, or $AB_2O_4$ where A and B are metal cations.[43,44] The extra peak around 39° 2$\theta$ value is attributed to a secondary rock-salt phase due to the presence of CuO (111),[45–48] where Cu is a divalent cation. The secondary rock salt (CuO) phase indicates that some of the copper has crystallized to form an FCC lattice, with the cations filling all $O_h$ sites.[49]

The full width at half maximum (FWHM) of the (311) peak of HESOx, HESOx-PVP, HESOx-SDS, and HESOx-CTAB are 0.2375, 0.1739, 0.2059, and 0.2119 $\theta$°, respectively, suggesting higher crystallinity in the surfactant-aided HESOx materials compared to the pristine HESOx. HESOx-PVP exhibits the

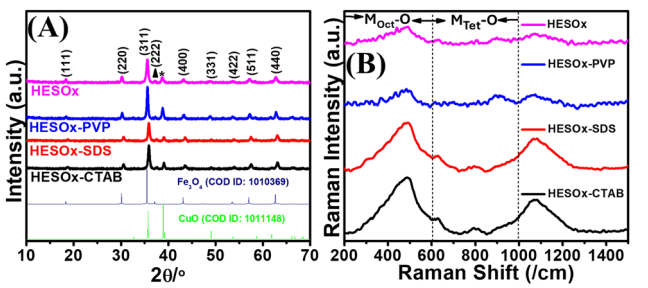


**Fig. 1** (A) XRD patterns, (B) Raman spectra of HESOx, HESOx-PVP, HESOx-SDS, and HESOx-CTAB.

highest crystallinity, evidenced by the lowest FWHM. There is a slight shift in the positions of the peaks of the HESOx-SDS, HESOx-CTAB, and HESOx-PVP to higher $2\theta^{\circ}$ angles relative to HESOx. This shift to higher angles suggests a decrease in the spacing (*d*-spacing) between atoms within the crystal lattice of the materials (lattice compression). In electrocatalysis, lattice compression and expansion can influence the electronic properties of the catalyst material, influencing its ability to facilitate certain chemical reactions at the electrodes. Studies have shown that lattice compression in certain electrocatalysts can enhance their activity for some reactions, such as $CO_2$ reduction.[50] However, HESOx-PVP's more expanded lattice relative to HESOx-SDS and HESOx-CTAB is an indication of the presence of more defects in HESOx-PVP, which facilitates water-splitting by enhancing the movement of reactants and products, thereby helping to overcome kinetic and mass transport limitations. The highest intensity for HESOx-PVP, while maintaining about the same position as the basic HESOx, shows that while PVP tries to maintain the properties of the basic HESOx, it enhances the crystallinity, thereby exposing more active sites for electrocatalysis.

The Raman spectra (Fig. 1B) indicate a complex vibrational structure typical of an inverse spinel with multiple transition metals. The peaks observed can be primarily due to the symmetric and asymmetric stretching modes of metal–oxygen bonds in both tetrahedral and octahedral sites. The strong peak around 490 $cm^{-1}$ is typical for the $F_{2g}$ mode of the spinel structure, related to the $O_h$ metal–oxygen vibrations. The peak around 629 $cm^{-1}$ could be a result of the M–O vibrations in the tetrahedral sites. The peak around 797 $cm^{-1}$ corresponds to the $A_{1g}$ mode, which involves symmetric stretching ("breathing") motion of the M–O bonds in the tetrahedral lattice sites of the spinel.[51–54] The bands around 900 $cm^{-1}$ are due to the interaction between the atoms in the tetrahedral and octahedral sites and give rise to oxygen vacancies at these sites during the high-temperature treatment. This may play a major part in surface gas absorption. The peak around 1100 is assigned to the second-order longitudinal optical (2LO) mode.[52,55] The peak intensity is dependent on the defect concentration. Defects such as vacancies, dislocations, or grain boundaries can scatter phonons (quantized vibrational energy) and disrupt the vibrational modes, leading to weaker Raman signals, as can be observed in the $F_{2g}$ peaks of HESOx and HESOx-PVP. A lower defect concentration means fewer disruptions, allowing for a more intense and sharper peak, as can be observed in the peaks of HESOx-SDS and HESOx-CTAB.[56] The presence of more defects in HESOx-PVP leads to a higher number and diversity of active sites and improved electronic properties, thereby creating a superior catalytic environment and making for better overall performance for the HER and OER.

The thermogravimetric analysis (TGA) of each sample is presented in Fig. S1A. The total mass loss percentages of HESOx, HESOx-PVP, HESOx-SDS, and HESOx-CTAB are approximately 4.26% at *ca.* 900.7 °C, 4.15% at *ca.* 900.7 °C, 4.75% at *ca.* 902.7 °C, and 3.57% at *ca.* 906.7 °C, respectively. The mass loss could be attributed to the burning of oxygen in the inert environment, leaving behind the metal residue. There is a slight dip around *ca.* 717 °C observed with the HESOx-SDS sample. This is likely due to the adsorbed nitrogen and sulfur molecules, which weaken the M–O (metal-to-oxygen) bonds and create more volatile species.

From the graphs of the first-order differential TGA (DTGA) (Fig. S1B), the peaks (maximum decomposition temperatures) are observed to be centered at 848.9 °C, 898.7 °C, and 855 °C for HESOx, HESOx-PVP, and HESOx-CTAB, respectively. The DTGA of HESOx-SDS shows an endothermic peak at 671.7 °C, which is likely due to the desorption/decomposition of the adsorbed organic moieties, particularly the SDS molecules adsorbed during the synthesis.[57]

The SEM images (Fig. S2A–D) reveal some very large particles in HESOx-SDS and HESOx-CTAB. A possible explanation for this is an insufficient concentration of surfactant to effectively coat all the forming particles, leading to aggregation and the formation of larger particles. The 0.5 wt% used may be insufficient for SDS and CTAB to effectively stabilize the particles, leading to Ostwald ripening and/or coalescence of the nanoparticles,[58–64] where the smaller particles in the suspension dissolve slightly and redeposit onto the larger particles. This mass transfer process, driven by the surface differences, would allow the bigger particles to grow at the cost of the smaller ones, leading to a broader size distribution/average particle size, and loss of electroactive surface area. The presence of the large crystals could lead to a wider particle-size distribution in HESOx-SDS and HESOx-CTAB. The TEM images of the samples are shown in Fig. 2A, B, and S3 along with their respective HRTEM images. The particle size distribution of each sample was obtained from the TEM image, and the mean particle sizes are 20.51 nm, 19.59 nm, 18.49 nm, and 12.92 nm for HESOx, HESOx-SDS, HESOx-CTAB, and HESOx-PVP, respectively. The larger mean particle sizes of HESOx-SDS and HESOx-CTAB are expected due to the coalescence of the particles, leading to a wide particle size distribution. The HRTEM analysis of the samples revealed the presence of multiple crystallographic planes characteristic of the inverse spinel structure. The observed planes included (222) (*d*-spacing = 0.24 nm), (220) (*d*-spacing = 0.31 nm), and (311) (*d*-spacing = 0.25 nm). The presence of the planes of MnO and CuO confirms the coexistence of secondary phases. The variation in observed planes across different samples may be attributed to compositional differences, processing conditions, or the subtle influence of synthesis parameters on crystallographic preferences.

The energy-dispersive X-ray (EDX) spectra of the samples (Fig. S4A–D) show the different elements of the samples, and the elemental mapping images from TEM (Fig. 2C, D, and S5A–D) suggest an even distribution of the elements across the samples. The specific surface area, pore size, and pore volume values of each sample (Table S1) were obtained from the single-point BET gas sorption analysis (GSA) method *via* nitrogen adsorption–desorption isotherm analysis, which is a well-known technique for the quick determination of the specific

 

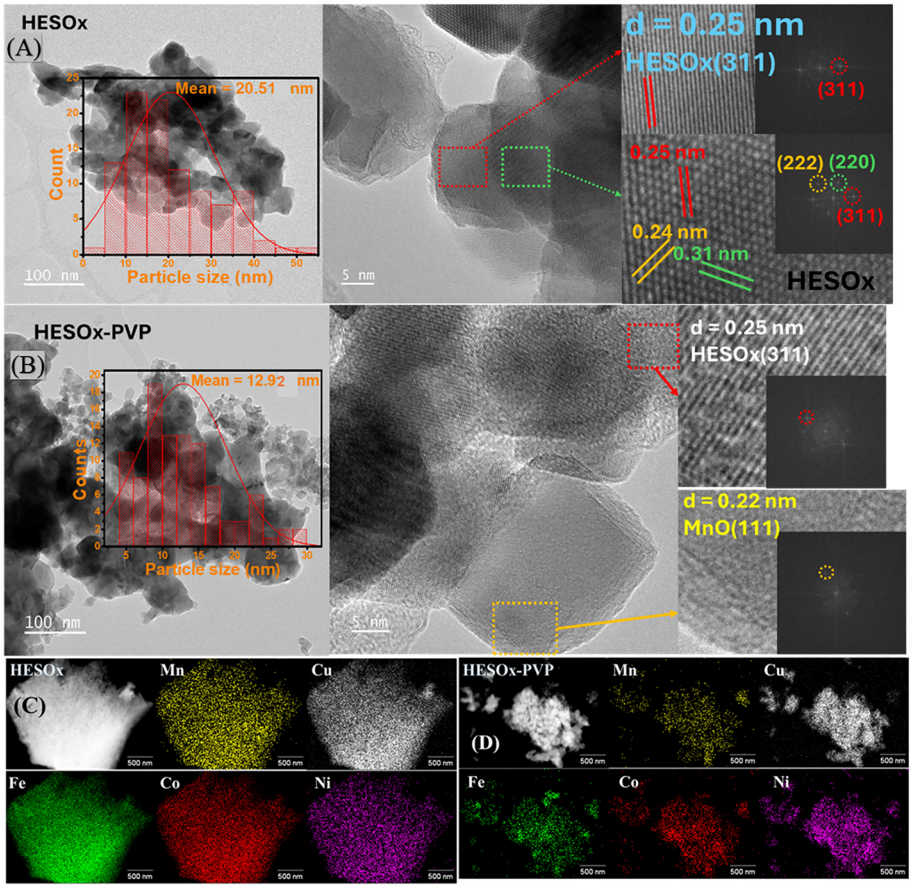


**Fig. 2** TEM and corresponding HRTEM images of (A) HESOx and (B) HESOx-PVP; TEM elemental mapping of (C) HESOx and (D) HESOx-PVP.

surface area (SSA) of nanomaterials.[65–69] The samples in descending order of SSA and pore volume values are HESOx-SDS, HESOx-CTAB, HESOx-PVP, and HESOx. The samples are seen to be mesoporous, with HESOx-PVP having the smallest pore size, which might make for better selectivity and could favor the hydrogen evolution reaction.[70]

The binding energies, chemical composition, and oxidation states of the chemical species on the surface of the samples were obtained using the XPS technique. The XPS survey (Fig. S6A) further confirms the presence of Co, Cu, Fe, Mn, Ni, and O in the materials.

As the oxidation state of each element changes, so does the number of unpaired electrons and hence the properties of the material. The peaks of the individual chemical species were extracted and deconvoluted to better understand the oxidation states of each element present in the sample. The scans of the chemical states of the different elements are shown in Fig. 3A–F & S6B. The O 1s spectra display three distinct components (Fig. 3A). In the HESOx sample, the peak due to oxygen atoms in the metal oxides (lattice oxygen ($O_L$)) is positioned at 529.65 eV. The peak around 531.71 eV is attributed to surface hydroxides ($OH^-$) and oxygen vacancies ($O_V$) in the samples. Oxygen vacancies are defects in a material's crystal structure, where there are missing oxygen atoms. This can influence the electrical, optical, and chemical properties of the material and enhance its catalytic activities. The peak at 533.16 eV is assigned to adsorbed water molecules or chemisorbed oxygen ($O_{ads}$).[65,71–74] HESOx-PVP has these O 1s peaks at 529.59 eV, 531.64 eV, and 533.18 eV. These peaks are at 529.79 eV, 531.68 eV, and 533.25 eV in HESOx-SDS, and 529.69 eV, 531.72 eV, and 533.20 eV in HESOx-CTAB. HESOx-PVP has the lowest binding energies for both $O_V$ and $O_L$ peaks compared to the others, which indicates higher electron density, indicating that both the lattice oxygen and defect oxygen are in the most electronically favorable state for electrocatalysis.

The intensities of the peak at *ca.* 531.7 (from the area under the peak) are in the order HESOx (14 767.68 cps eV) > HESOx-SDS (12 412.58 cps eV) > HESOx-PVP (8241.13 cps eV) > HESOx-CTAB (6906.64 cps eV) (Table S2A). However, the intensity of this peak could be influenced by surface contaminants such as adventitious carbon. The $O_{ads}$ (C═O) peak intensities are in the order HESOx > HESOx-SDS > HESOx-PVP > HESOx-CTAB (Table S2A). The $O_V/O_L$ ratio is an indicator of the relative amount of surface defect sites with low oxygen coordination.[75] The $O_V/O_L$ ratios for HESOx, HESOx-PVP, HESOx-SDS, and HESOx-CTAB are 1.00, 0.56, 0.79, and 0.68, respectively, and their respective overall surface contaminant percentages are 29.42%, 19.12%, 22.82%, and 25.28%. Hence, while

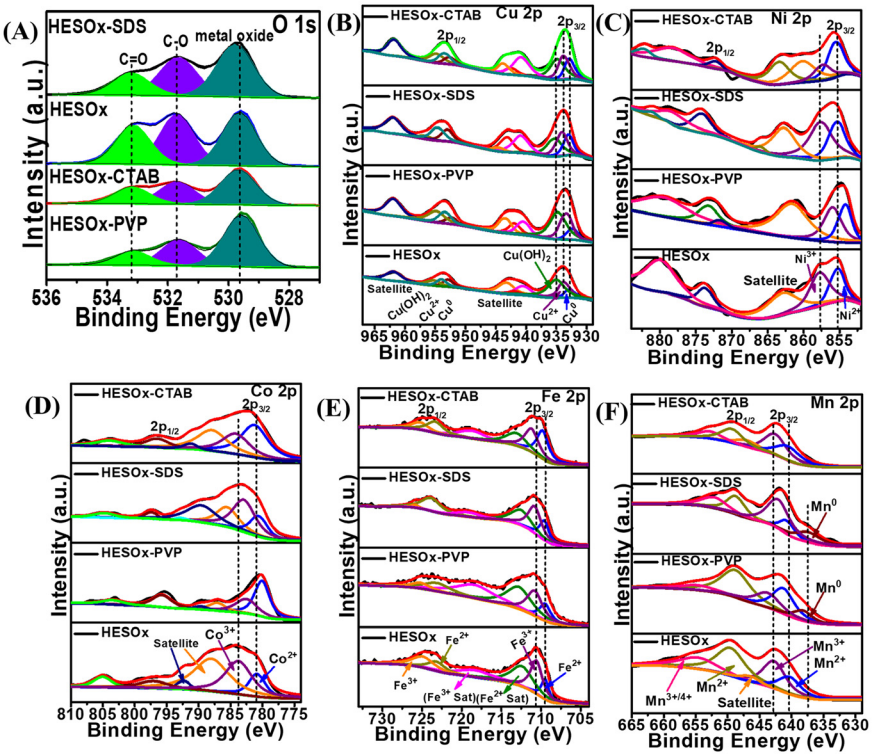


**Fig. 3** XPS scans of HESOx, HESOx-PVP, HESOx-SDS, and HESOx-CTAB showing the (A) O 1s, (B) Cu 2p, (C) Ni 2p, (D) Co 2p, (E) Fe 2p, and (F) Mn 2p scans.

HESOx-PVP has fewer intrinsic defects ($O_V/O_L$ ratio), it has the least amount of surface contaminants, which means that a significant portion of its active sites are exposed and accessible for electrocatalysis. The C 1s scans (Fig. S6B) support this finding, as HESOx-PVP has the least peak intensity among the four samples.

The Cu 2p scans (Fig. 3B) show asymmetric peaks corresponding to Cu $2p_{3/2}$ and Cu $2p_{1/2}$. In HESOx, these peaks are around 934.08 and 953.84 eV, respectively, with a spin–orbit splitting of *ca.* 19.76 eV. These binding energies are close to those observed in CuO.[47,76,77] The peak separation of 19.76 eV suggests the presence of Cu in the divalent and lower valence states in the materials.[78] The presence of shakeup (satellite) peaks at *ca.* 940–942 (triplet) and 962 eV confirms the presence of $Cu^{2+}$.[79,80] As seen in Fig. 3B, the Cu $2p_{3/2}$ and Cu $2p_{1/2}$ of HESOx-PVP are positioned at 933.74 eV and 953.67 eV, respectively. Interestingly, this shift to lower binding energies, observed only in HESOx-PVP, signifies an increase in its electron density and a less stable nucleus, which could enhance the ability of HESOx-PVP to interact with water molecules, potentially improving its electrocatalytic activity. For HESOx-SDS, the Cu $2p_{3/2}$ and Cu $2p_{1/2}$ are around 934.12 and 954.06 eV, respectively, which signifies a loss of electron density. HESOx-CTAB has these peaks at 933.72 eV and 953.60 eV. The deconvolution of the Cu $2p_{3/2}$ and Cu $2p_{1/2}$ states displays three peaks each. The peaks of Cu $2p_{3/2}$ and Cu $2p_{1/2}$ around 932.7 and 952.8 eV, respectively, are due to Cu in the metal state. The peaks around 933.7 and 953.9 eV are due to divalent copper species, which are due to CuO on the surface of the catalyst,[78,80,81] while the two Cu $2p_{3/2}$ and Cu $2p_{1/2}$ peaks at *ca.* 935 and 955 eV, respectively, are attributed to $Cu(OH)_2$ due to the presence of $NH_4OH$ in the synthesis.[82]

The Ni 2p spectra (Fig. 3C) of the samples show two asymmetric peaks around 855 and 873 eV, consistent with the Ni $2p_{3/2}$ and Ni $2p_{1/2}$ species, respectively, as well as satellite peaks which are due to multiple splitting in the Ni energy levels. The satellite peaks confirm the existence of divalent nickel.[83–85] The HESOx Ni $2p_{3/2}$ peak features a doublet, with peaks at 855.37 and 857.78 eV attributed to the $Ni^{2+}$ and $Ni^{3+}$ oxidation states, respectively, which are consistent with NiO and $Ni(OH)_2$. These peaks are at 854.28 and 855.95 eV in HESOx-PVP, 855.40 and 857.62 eV in HESOx-SDS, and 855.54 and 857.34 eV in HESOx-CTAB.[86,87] Again, as in Cu 2p spectra, the peaks of HESOx-PVP show significant shifts to lower binding energies, while those of HESOx-CTAB and HESOx-SDS show no detectable shift from those of HESOx. This result shows that HESOx-PVP possesses rich electron density compared to its counterparts, which could imply more efficient electrocatalysis.

The Co 2p scans are displayed in Fig. 3D. The HESOx sample has two peaks at about 783.4 and 797.4 eV, consistent with Co $2p_{3/2}$ and Co $2p_{1/2}$, respectively,[72,88–90] with an energy splitting of 13.69 eV and a satellite at 805.04 eV. The deconvoluted Co $2p_{3/2}$ comprises peaks positioned at 780.83 eV and 783.75 eV attributed to $Co^{2+}$ and $Co^{3+}$ oxidation states, respectively. Along with these peaks are satellite peaks around 788.01 and 792.39 eV, suggesting the presence of $Co_3O_4$ and CoO. The

Co $2p_{3/2}$ and Co $2p_{1/2}$ peaks of HESOx-PVP are at 780.06 and 795.77 eV, with an energy splitting of 15.70 eV, and satellite peaks at 787.07, 789.60, and 803.43 eV. The Co $2p_{3/2}$ peak has a shoulder at 782.47 eV. The Co $2p_{3/2}$ and Co $2p_{1/2}$ peaks of HESOx-SDS are at 783.01 and 797.49 eV, respectively, with an energy splitting of 14.48 eV and a satellite peak at 804.73 eV. The deconvoluted Co $2p_{3/2}$ features peaks at 780.580 and 782.91 eV, accompanied by satellite peaks at 785.52 and 789.53 eV. The HESOx-CTAB samples have Co $2p_{3/2}$ and Co $2p_{1/2}$ peaks at about 782.10 and 796.53 eV, respectively, with an energy splitting of 14.44 eV and a satellite at 803.95 eV. The deconvoluted Co $2p_{3/2}$ comprises peaks positioned at 781.24 and 784.20 eV attributed to $Co^{2+}$ and $Co^{3+}$ oxidation states, respectively. Along with these peaks are satellite peaks at 787.92 and 791.28 eV. In summary, the peaks of HESOx-PVP shift to higher binding energies compared to other HESOx materials, suggesting increased electron density.

From the Fe 2p scans (Fig. 3E), two peaks are present around 710.4 and 724.6 eV, corresponding to the Fe $2p_{3/2}$ and Fe $2p_{1/2}$ species. Given the position of these two peaks, a hematite ($Fe_2O_3$) structure is more likely than a magnetite ($Fe_3O_4$) structure.[74,91–93] The peak around 710.4 eV suggests the presence of $Fe_2O_3$, $Fe_3O_4$, $Fe(OH)_3$, or FeOOH, while the one at ~724.6 eV is due to the presence of ferric oxides (Fe (III)).[77] In the HESOx sample, the Fe $2p_{3/2}$ peak positions for $Fe^{2+}$ and $Fe^{3+}$ are at *circa* 709.49 and 710.59 eV, respectively, and the Fe $2p_{1/2}$ peaks of $Fe^{2+}$ and $Fe^{3+}$ appear at 723.19 and 724.89 eV, respectively. The presence of the $Fe^{2+}$ and $Fe^{3+}$ species indicates partial oxidation of the samples. Satellite peaks of $Fe^{2+}$ and $Fe^{3+}$ appear at 712.41 and 718.38 eV, respectively.[94] From the peak areas, the proportions of $Fe^{2+}$ and $Fe^{3+}$ in the Fe $2p_{3/2}$ peak are 47.9% and 52.1%, respectively. HESOx-PVP has the Fe $2p_{3/2}$ peaks at 709.49 and 710.81 eV, corresponding to $Fe^{2+}$ and $Fe^{3+}$, respectively. These peaks are at 709.59 and 710.81 eV, respectively, for HESOx-SDS, and at 709.81 and 711.20 eV, respectively, for HESOx-CTAB. In summary, there is no significant shift in peak for all the HESOx materials, suggesting that Fe is redox-silent in this work.

The Mn 2p scans are shown in Fig. 3F. A doublet is observed due to spin–orbit splitting, with energies at 641.79 and 649.85 eV for HESOx, corresponding to the 3/2 and 1/2 states, respectively, with a spin–orbital splitting of around 8.06 eV. The very broad peaks could be due to multiple oxidation states and suggest the presence of $Mn_3O_4$, as it consists of mixed oxidation states, $Mn^{2+}$ and $Mn^{3+}$. The presence of a satellite peak at 646.56 eV is attributed to the multiple oxidation states. The deconvoluted Mn $2p_{3/2}$ and Mn $2p_{1/2}$ peaks consist of two components with binding energy values of 640.3 ($Mn^0$; $Mn^{2+}$) and 642.7 eV ($Mn^{3+}$) for the Mn $2p_{3/2}$ and the Mn $2p_{1/2}$ has peaks at 649.5 ($Mn^{2+}$) and 654.6 eV ($Mn^{3+}$, $Mn^{4+}$, or a higher oxidation state, such as $Mn^{7+}$).[71,72,85,95–99] The Mn $2p_{3/2}$ and Mn $2p_{1/2}$ peaks of HESOx-PVP are positioned at 641.45 and 648.85 eV, respectively, with an energy splitting of around 7.39 eV. The deconvoluted Mn $2p_{3/2}$ consists of peaks at 638.21 ($Mn^0$), 641.28 ($Mn^{2+}$), and 643.74 eV ($Mn^{3+}$), while those of the Mn $2p_{1/2}$ are at 648.77 and 654.65 eV. HESOx-SDS has Mn $2p_{3/2}$ and Mn $2p_{1/2}$ peaks at 641.30 and 649.44 eV, respectively, with an energy splitting of around 8.14 eV, and the appearance of a satellite peak at 646.14 eV. The deconvoluted Mn $2p_{3/2}$ consists of peaks at 637.40 ($Mn^0$), 640.70 ($Mn^{2+}$), and 642.11 eV ($Mn^{3+}$), while those of Mn $2p_{1/2}$ are at 648.72 and 652.09 eV. HESOx-CTAB has Mn $2p_{3/2}$ and Mn $2p_{1/2}$ peaks at 641.87 and 649.38 eV, respectively, with an energy splitting of around 7.5 eV, and the appearance of a satellite peak at 646.98 eV. The deconvoluted Mn $2p_{3/2}$ consists of peaks at 640.62 ($Mn^0$; $Mn^{2+}$) and 642.61 eV ($Mn^{3+}$), while those of the Mn $2p_{1/2}$ are at 649.34 and 652.77 eV. All four samples suggest the presence of $Mn_3O_4$ (broad peaks, $Mn^{2+}$, $Mn^{3+}$) and the likelihood of $MnO_2$ ($Mn^{4+}$). In summary, the HESOX-PVP shows a slight shift to the higher binding energy, indicating decreased electron density.

In general, the XPS data show the unique influence of PVP on the electronic structure of HESOx. Compared to the other samples, the Cu 2p, Co 2p, Fe 2p and Ni 2p electronic states of HESOx-PVP generally appear at lower binding energies, while Mn 2p shifted to higher binding energies, indicating that Cu, Co, Fe, and Ni gain electron density and have a weaker effective nuclear charge, while the reverse is the case for Mn.[100] Although HESOx is expected to possess unique but complicated electronic structure due to the different cations, it is interesting to observe that PVP further aids this electronic complication. One expects this electronic modulation to facilitate the transfer of electrons and promote the HER process.

The electronic structure, including the position of the Fermi level relative to the band edges, influences electrocatalytic activity. The valence band spectra of the XPS are presented in Fig. 4. The energy difference between the Fermi level and the valence band maximum ($E_F - E_{VBM}$), like the d-band center, can provide an insight into the electronic structure of the transition metals of the HESOx and its impact on the electrocatalytic properties. For example, a larger $E_F - E_{VBM}$ value means a weaker interaction between the d-states and the Fermi

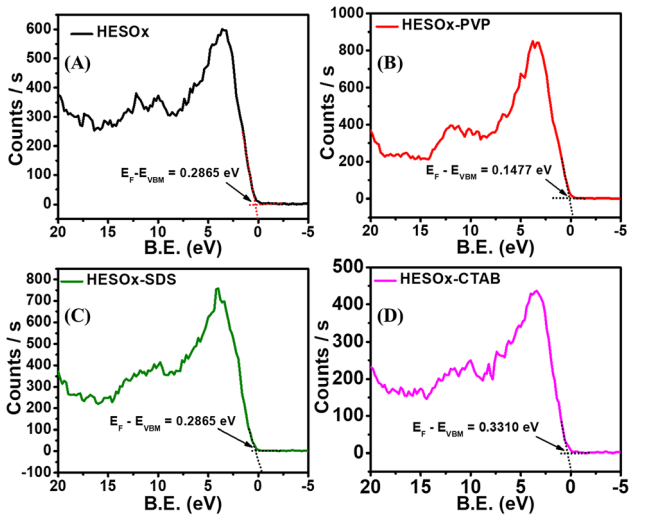


**Fig. 4** Valence band XPS spectra of (A) HESOx, (B) HESOx-PVP, (C) HESOx-SDS, (D) HESOx-CTAB.

level, which can influence the adsorption and reaction of molecular intermediates. Here, the estimated values of the $E_F - E_{VBM}$ are 0.2865, 0.1477, 0.2865, and 0.3310 eV for HESOx, HESOx-PVP, HESOx-SDS, and HESOx-CTAB, respectively. The smaller value of the HESOx-PVP means that its electrons are at a relatively lower energy compared to the others,[75,101,102] indicating a stronger interaction between its d-states and the Fermi level. This indicates that HESOx-PVP could optimize the HER/OER performance by lowering the reaction energy barrier and enhancing the electronic interaction with the reaction intermediates. This corroborates the findings in Fig. 3.

### Electrochemical tests

To activate the electrodes and obtain information about the redox behavior of the multi-metal electrocatalyst, cyclic voltammograms (Fig. 5A) of the RDE modified with the electrocatalysts were obtained at a scan rate of 25 mV $s^{-1}$ at ambient temperature. Hydrogen adsorption/desorption peaks occur at the potential region between 0.1 and 0.2 V *vs.* RHE. The oxidation and reduction signatures of the transition metal oxides are found between 0.3 V and 1.25 V *vs*. RHE. These peaks are due to the reversible and continuous electrochemical reactions happening at the electrode–electrolyte interface, signifying pseudocapacitive behaviors.[103,104] The electrochemically active surface area (ECSA) is a critical parameter for determining how much of the exposed surface of the electrocatalyst is available for electrochemical activity. To determine the ECSA, cyclic voltammograms obtained at the non-faradaic region of the catalysts at different scan rates (10–70 mV $s^{-1}$) were plotted (Fig. 5B–E). The double-layer capacitance ($C_{dl}$) is obtained from the slope of the plot of current density differences ($\Delta J/2 = (J1 - J2)/2$) between the upper current density ($J1$) and lower current density ($J2$) in the middle of the potential window against the scan rates, or by plotting the anodic current density ($J1$) and cathodic current density ($J2$) and obtaining the average of absolute values of the slopes (Fig. 5F), where $J1$ is the anodic current ($I_{pa}$) and $J2$ is the cathodic current ($I_{pc}$).

The ECSA was then determined using the equation:

$$\text{ECSA} = \frac{C_{dl} \times \text{geometric surface area}}{C_s} \quad (1)$$

where $C_{dl}$ is the double-layer capacitance of electrocatalysts, and $C_s$ is the specific capacitance of the glassy carbon rotating disk electrode (RDE).[105,106] For the $C_s$, we used a general value of 0.040 mF $cm^{-2}$.[105,107–109] The $C_{dl}$ and ECSA values of the electrocatalysts are summarized in Table S3. The larger ECSA of HESOx-PVP suggests that, regardless of the total surface area provided by the GSA, HESOx-PVP has a greater portion accessible to electrocatalytic reactions than other samples.

The HER curves (Fig. 6A) were obtained from LSV measured at room temperature with a scan rate and a rotation rate of 10 mV $s^{-1}$ and 1600 rpm, respectively. A comparison of the overpotentials of the samples is shown in Fig. 6B and summarized in Table S4. HESOx-PVP exhibits a better HER performance than the other samples, reaching 10 mA $cm^{-2}$ at an overpotential of 87 mV. The smaller overpotential suggests a more efficient HER with HESOx-PVP. These findings are consistent with the XPS analysis, indicating a correlation between lower binding energies and enhanced HER performance.

To investigate the HER mechanism, the Tafel slopes were determined from the Tafel plots shown in Fig. 6C, and the values indicate that the electrocatalysis proceeds through the Volmer–Heyrovsky pathway (eqn (2) and (3)):[110–114]

$$H_2O + e^- + M \leftrightarrow M\text{–}H_{ads} + OH^- \text{(Volmer)} \quad (2)$$

$$H_2O + e^- + M\text{–}H_{ads} \leftrightarrow H_2 + OH^- \text{(Heyrovsky)} \quad (3)$$

where "M" denotes an available site on the electrocatalyst's surface, and M–$H_{ads}$ denotes the hydrogen atoms adsorbed. The HER kinetics of electrocatalysts depends on the strength

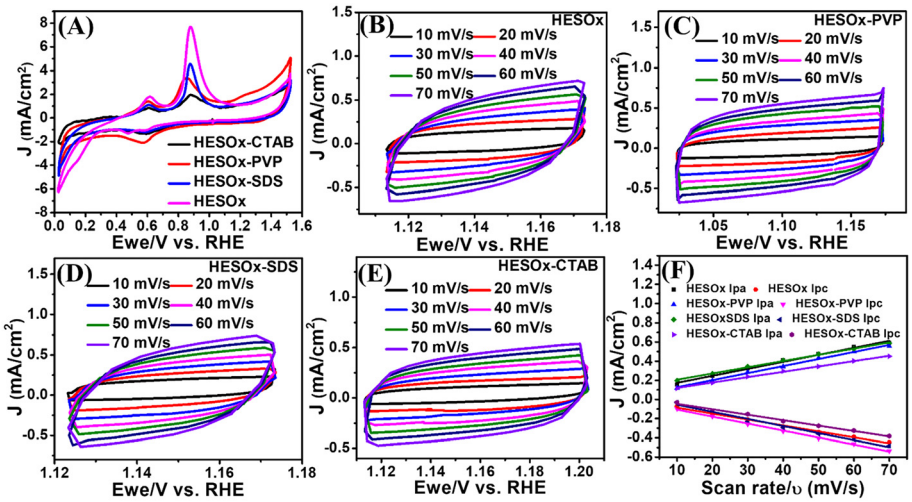


**Fig. 5** (A) Cyclic voltammograms in 1 M KOH at 25 mV $s^{-1}$, (B–E) CV scans of the non-faradaic region of the samples at different scan rates in 1 M KOH, and (F) their corresponding linear plots.

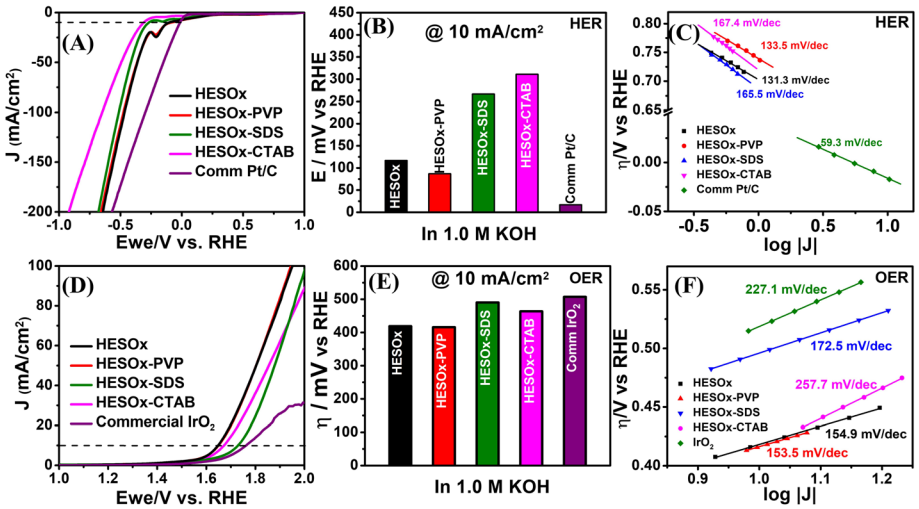


**Fig. 6** (A) HER polarization curves in 1.0 M KOH at 10 mV $s^{-1}$ and 1600 rpm, (B) HER overpotential at 10 mA $cm^{-2}$ of the electrocatalysts, (C) HER Tafel plots, (D) OER polarization curves in 1.0 M KOH at 10 mV $s^{-1}$ and 1600 rpm, (E) OER overpotential at 10 mA $cm^{-2}$ of the electrocatalysts, (F) OER Tafel plots.

of the M–$H_{ads}$ bonds, and the M–$H_{ads}$ bonds formed on the electrocatalysts, according to Sabatier's principle, should not be too strong or too weak to promote the efficient adsorption and desorption of M–$H_{ads}$ intermediate and the release of $H_2$.[115]

Similarly, the OER activity of HESOx-PVP is the best of the four samples, attaining a current density of 10 mA $cm^{-2}$ at an overpotential of 415.8 mV, compared to 419, 463.7, 490.3, and 507.2 mV required by HESOx, HESOx-CTAB, HESOx-SDS, and $IrO_2$, respectively. From the Tafel slopes (Fig. 6D), HESOx-PVP shows the lowest value (153.5 mV $dec^{-1}$) among all the synthesized catalysts and commercial $IrO_2$, indicating the best OER kinetics.

### Metal salt-to-PVP ratio studies

Based on the HER and OER performances, PVP was selected for further studies. Different wt% of PVP (1–50%) were used as templates in the synthesis of the HESOx using the same method specified above for the HESOx-SAS materials. XRD and Raman (Fig. S7) show the same signatures as obtained in the HESOx materials above. From the GSA (Table S5), the SSA of $HESOx_{PVP\ 1\%}$ (21.8 $m^2\ g^{-1}$) and its pore volume are higher than those of the other prepared catalysts. The $C_{dl}$ values were obtained from the non-faradaic cyclic voltammograms in Fig. S8 and the linear plots in Fig. S9. The $C_{dl}$ and ECSA values are summarized in Table S6. The larger ECSA of $HESOx_{PVP\ 1\%}$ suggests that it has a greater portion accessible to electrocatalytic reactions than other samples. The different PVP-assisted materials were compared in 1 M KOH with a three-electrode setup and 10 mV $s^{-1}$ scan rate to determine the optimal ratio for HER and OER.

The HER polarization curves (Fig. 7A) show that the $HESOx_{PVP\ 1\%}$ exhibits a high HER activity, requiring 16 mV to reach 10 mA $cm^{-2}$. A comparison of the overpotentials of the samples is shown in Fig. 7B and summarized in Table S7. The HER polarization curves feature reduction peaks around −0.25 V *vs.* RHE. Cyclic voltammetry was performed to obtain a reverse scan (Fig. S10) to study the complementary hydrogen oxidation reaction (HOR). The presence of anodic peaks around −18 mV *vs.* RHE in the reverse scan of the Linear Sweep Voltammetry (LSV) curves suggests that the materials are active for Hydrogen Oxidation Reaction (HOR) ($H_2 + 2OH^- \rightarrow 2H_2O + 2e^-$). Therefore, the detailed investigation of the material's electrocatalytic activity and kinetics towards the HOR will be the focus of future research.

The HER Tafel slopes are compared in Fig. 7C. All the prepared samples have Tafel slopes above 40 mV $dec^{-1}$, suggesting that the HER follows the Heyrovsky–Volmer pathway on all the samples, where the Volmer step is the rate-determining step.[116] From the mass activity of each catalyst (Fig. 7D) obtained at −0.25 V (*vs.* RHE) from the LSV curves in Fig. 7A, $HESOx_{PVP\ 1\%}$ has a mass activity of 24.72 mA $mg_{metal}^{-1}$, which is better than the other prepared catalysts. Moreover, the electrochemical impedance spectra (EIS) (Fig. 7E) suggest that $HESOx_{PVP\ 1\%}$ has a higher charge transfer efficiency than all the other synthesized samples (Table S8). During continuous HER at 10 mA $cm^{-2}$ for 15 h (Fig. 7F), $HESOx_{PVP\ 1\%}$ is seen to be quite stable, with the overpotential slightly shifting to less negative values. The prolonged operation under constant current might have facilitated an *in situ* surface activation in the high-entropy inverse spinel oxide. After 2000 CV cycles, the overpotential at 10 mA $cm^{-2}$ shifted negatively by 11 mV after 2000 cycles (to 27 mV) (Fig. 7F inset). The shift to higher overpotentials is commonly associated with poor kinetics. Extended cycling usually leads to the formation of surface films, leading to loss of electrical conductivity.

Similarly, a comparison of the OER of the electrocatalysts (Fig. 8A) clearly shows that $HESOx_{PVP\ 1\%}$ exhibits the highest OER activity compared to the other electrocatalysts and com-

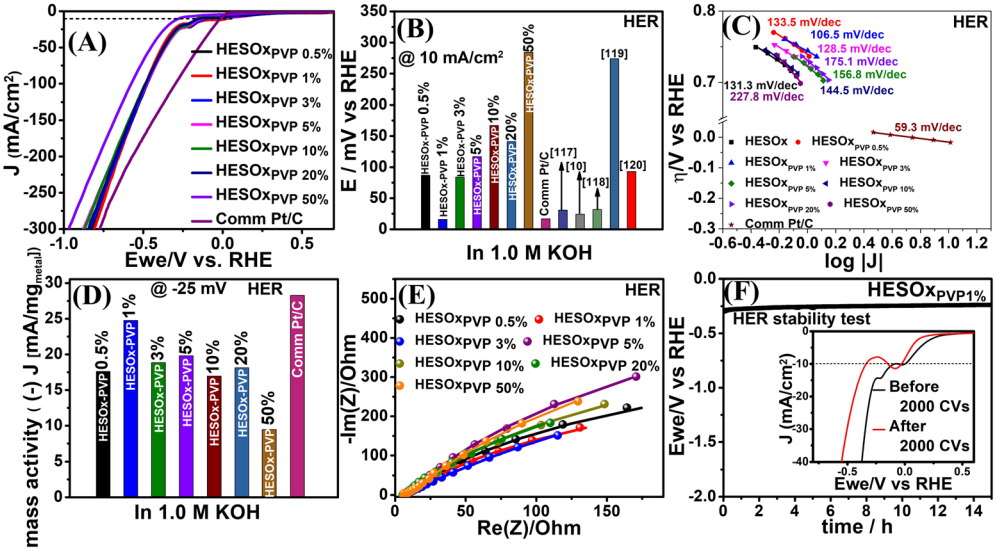


**Fig. 7** (A) HER polarization curves at 10 mV $s^{-1}$ scan rate and a rotation rate of 1600 rpm in 1.0 M KOH, (B) a comparison of the overpotential at 10 mA $cm^{-2}$ in comparison with literature,[10,117–120] (C) Tafel plots of the electrocatalysts, (D) mass activity of these catalysts at −0.25 V *vs.* RHE, (E) EIS Nyquist plots @ −0.77 V, (F) chronopotentiometric test of $HESOx_{PVP\ 1\%}$ at −10 mA $cm^{-2}$ in 1.0 M KOH for 15 h (inset: LSVs before and after 2000 CVs).

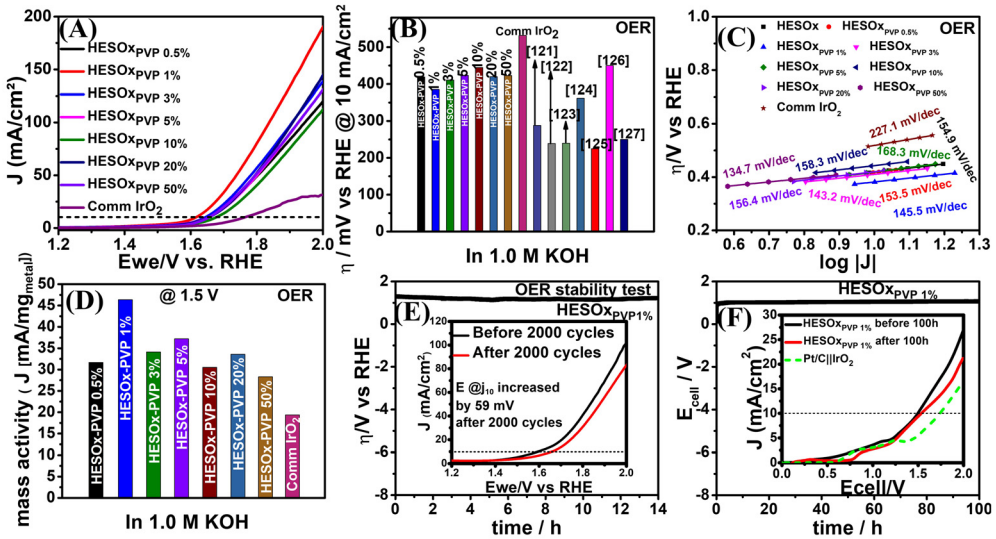


**Fig. 8** (A) OER polarization curves at 10 mV $s^{-1}$ scan rate and a rotation rate of 1600 rpm in 1.0 M KOH, (B) overpotential of the catalysts at 10 mA $cm^{-2}$ compared with literature.[121–127] (C) Tafel plots of these catalysts, (D) mass activity of the catalysts at 1.5 V *vs.* RHE, (E) chronopotentiometric test of $HESOx_{PVP\ 1\%}$ at 10 mA $cm^{-2}$ in 1.0 M KOH for 15 h, (F) overall water splitting long-term durability test at 10 mA $cm^{-2}$. Inset: polarization curves before and after the durability test.

mercial $IrO_2$. The respective overpotentials at 10 mA $cm^{-2}$ of the samples are shown in Fig. 8B and summarized in Table S7. The Tafel slopes are compared in Fig. 8C. The mass activity (Fig. 8D) of each catalyst was calculated at 1.5 V *vs.* RHE from its LSV curve in Fig. 8A. The OER mass activity of $HESOx_{PVP\ 1\%}$ is 46.37 mA $mg_{metal}^{-1}$, which is better than other catalysts and commercial $IrO_2$. After 2000 CV cycles, the overpotential at 10 mA $cm^{-2}$ shifted positively by 59 mV after 2000 cycles (to 444 mV). However, chronopotentiometry (Fig. 8E) run at 10 mA $cm^{-2}$ shows that $HESOx_{PVP\ 1\%}$ is fairly stable as the overpotential shifts negatively by 69 mV over 14 h.

Based on the HER and OER performance, the potential water-splitting performance of $HESOx_{PVP\ 1\%}$ was evaluated using a two-electrode setup as depicted in Scheme S5.[10,116] Two 5 cm × 1 cm carbon cloth strips were used for the anode and cathode. The catalyst ink was prepared by dispersing 10 mg of $HESOx_{PVP\ 1\%}$ and 10 mg of OLC in 500 μL of ethanol (99.99% absolute ethanol) and 20 μL of Nafion (5 wt%) and

sonicated for 30 min. 120 μL of the ink was loaded on a 1 cm × 1 cm area of each carbon cloth. LSV was obtained at 5 mV $s^{-1}$. In comparison to the 1.74 V achieved by commercial Pt/C||$IrO_2$ catalyst combination, $HESOx_{PVP\ 1\%}$ shows a superior performance, requiring a potential of ~1.497 V to reach 10 mA $cm^{-2}$ (Fig. 8F inset) and is comparable to literature (Table S9).[10,116,119,128–133] Under a constant current of 10 mA $cm^{-2}$, $HESOx_{PVP\ 1\%}$ works stably with ~13% increase in potential over a 100-hour testing period (Fig. 8F). LSV collected after 100 hours shows only a little increase in the potential required (1.53 V) to reach 10 mA $cm^{-2}$.

### The effect of Cu

Besides HEAs, other categories of alloys based on their configurational entropy $\Delta S_{conf}$ include low entropy alloys (LEAs) and medium entropy alloys (MEAs). LEAs consist of one or two primary elements and the configurational entropy, $\Delta S_{conf} \leq 0.69R$, while MEAs comprise a mix of three or four primary elements and $0.69R \leq \Delta S_{conf} \leq 1.61R$.

While multi-principal element alloy systems (MEAs and HEAs) and their oxides have received a lot of attention as electrocatalysts for various applications, more attention is concentrated on high-entropy materials than on medium-entropy materials.[12,134–136]

Moreover, Cu-based materials have shown outstanding electrocatalytic activity and great stability and have been a center of research for applications such as HER, OER, ammonia sensing, $CO_2$ reduction, and hydrogen storage.[137–143] In this section, we compare the physical properties and the effect of the presence and absence of copper (Cu) high- and medium-entropy spinel oxides $(CuCoFeMnNi)_3O_4$ (HESOx) and $(CoFeMnNi)_3O_4$ (MESOx), synthesized *via* reverse co-precipitation and calcination, as discussed earlier[39] (excluding the salt of Cu in the MESOx mix) as well as their behaviors towards alkaline water splitting.

### Physicochemical characterizations

The XRD (Fig. 9A) reveals peaks centered around 2$\theta$° values of 18.42°, 30.28°, 35.65°, 37.22°, 43.31°, 53.72°, 57.26°, and 62.87° for HESOx, and 18.52°, 30.31°, 35.71°, 37.32°, 43.37°, 54.08°, 57.32°, and 62.89° for MESOx and are attributed to the reflections from the planes of (111), (220), (311), (222), (400), (422), (511), and (440), and the high-intensity peak at (311), suggests an inverse spinel structure,[144–146] consistent with the patterns of $Fe_3O_4$ (COD ID 1010369). The slight shift to the left of HESOx suggests that the addition of Cu introduces lattice expansion. The peaks of HESOx are also seen to be broader than the peaks of MESOx, suggesting higher crystallinity of the MESOx particles. The FWHM values of the (311) planes of HESOx and MESOx are 0.4638 2$\theta$° and 0.2684 2$\theta$°, respectively, suggesting smaller particle sizes in HESOx than in MESOx. The minor traces observed in the patterns of MESOx match the phase of $Fe_2O_3$ and are consistent with COD ID 1011240, while the minor traces observed in HESOx match the CuO phase and are consistent with COD ID 1011148.

The Raman spectra (Fig. 9B) show almost similar signatures for HESOx and MESOx. Both spectra exhibit the characteristic $E_g$, $F_{2g}$, and $A_{1g}$ Raman active modes of $AB_2O_4$ spinels, corresponding to metal–oxygen (M–O) vibrations at tetrahedral (A-site) and octahedral (B-site) cation sites.[38] Cu addition seems to promote site preference, giving rise to reduced cation disorder and leading to better-defined peaks in HESOx. In contrast, the peaks of MESOx appear broader and merged, suggesting higher cation disorder arising from random A/B site occupancy, suggesting a higher defect density in MESOx. The splitting of the $E_g$ mode in HESOx indicates local octa-

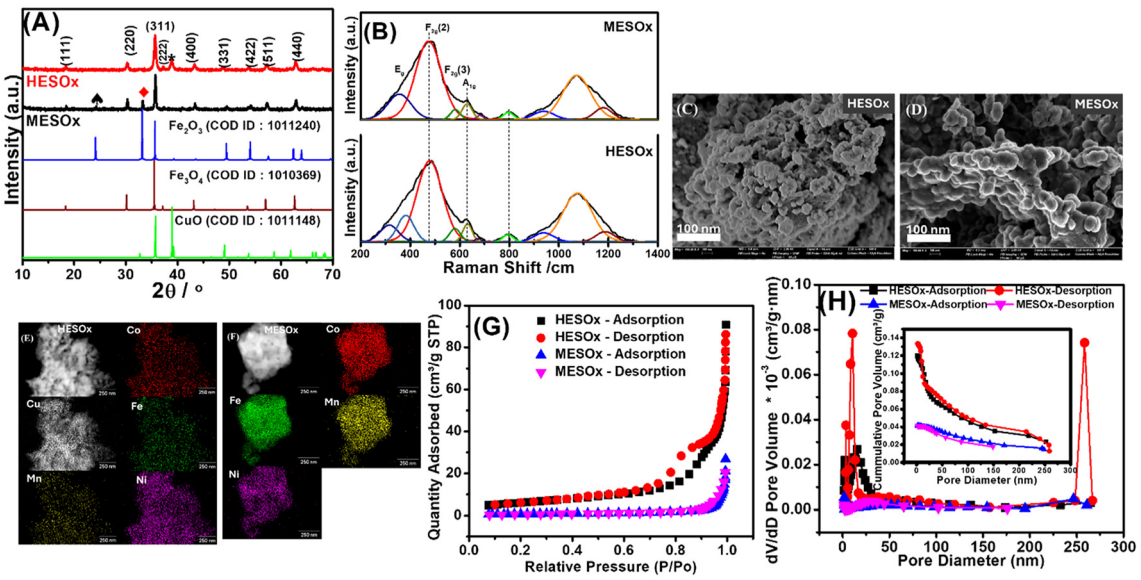


**Fig. 9** (A) XRD patterns, (B) Raman spectra, (C and D) SEM and (E and F) elemental mapping of the samples. (G) Adsorption–desorption isotherm plots of the samples. (H) Pore size distribution plots.

hedral distortion, which creates more active sites for the adsorption of reaction intermediates.[147,148] The main $F_{2g}(2)$ band (~470–490 $cm^{-1}$) also appears at slightly higher wavenumber in HESOx relative to MESOx, indicating shorter M–O bond lengths, and suggesting stronger bonding. The sharper $A_{1g}$ peak in HESOx compared to MESOx indicates a higher degree of structural order and crystallinity and more stable tetrahedral networks, which could lead to more efficient electron transfer. The $A_{1g}$ mode (~680 $cm^{-1}$) is also shifted upward, emphasizing the bond strength.

The SEM images in Fig. 9C and D show spherical crystals with smaller particle sizes of the HESOx material, suggesting a larger surface area than in the MESOx. The EDS mapping images (Fig. 9E and F) show a uniform distribution of the elements across the samples.

The GSA agrees with the SEM, revealing surface area values of 21.25 $m^2$ $g^{-1}$ for HESOx and 2.8 $m^2$ $g^{-1}$ for MESOx, suggesting more potential active sites for reactions on HESOx. HESOx is also more porous with a pore volume of 0.06 $cm^3$ $g^{-1}$ compared to 0.01 $cm^3$ $g^{-1}$ of MESOx. The samples are mesoporous, with the HESOx sample having a smaller pore size of 11.36 nm compared to the value of 15.77 nm for MESOx. These values suggest superior electrocatalytic performance with HESOx than MESOx.

According to the IUPAC classification, both samples display type-IV features, which suggests the presence of mesopores in the samples, as shown by the adsorption–desorption isotherm plots in Fig. 9G. The type H3 hysteresis loop, associated with the presence of slit-like pores, is observed in MESOx. The absence of the limiting step observed in mesoporous sorbents of type-IV isotherm at high relative pressure suggests an incomplete pore filling. In contrast, the type-H2 hysteresis observed in HESOx indicates bottleneck constrictions and is associated with disordered materials where the pore size and shape distribution are not well defined.[149–151]

The as-synthesized spinel materials exhibited a narrow pore-size distribution, which is centered at 10 nm (Fig. 9H). Meanwhile, a higher cumulative pore volume is observed with the addition of Cu in the mix (inset of Fig. 9H).

The TEM images (Fig. 10A and B) confirm the smaller particle sizes of HESOx, with an average particle size of 13.65 nm, smaller than the average particle size (74.45 nm) of MESOx. This corroborates the broader (311) peak and SEM images. The HRTEM micrographs (Fig. 10C and D) show the *d*-spacing values corresponding to the (111), (220), (311), and (222) planes and agree with the XRD patterns.

The chemical compositions and oxidation states of the spinels were investigated using X-ray photoelectron spectroscopy (XPS) analyses, shown in Fig. 11.

The Co 2p peak of MESOx at 779.94 eV is attributed to the $Co^{2+}$ oxidation state, and the other at 782.21 eV is attributed to the $Co^{3+}$ state at 782.21 eV.[72,88–90] In the Fe 2p scan, the peak at 709.42 eV corresponds to $Fe^{2+}$ and the peak at 710.47 eV corresponds to $Fe^{3+}$.[74,92,93] In the Ni 2p scan of MESOx, the peak corresponding to $Ni^{2+}$ is positioned at 855.53 eV, while $Ni^{3+}$ is positioned at 857.27 eV.[84,137] The peak at 640.76 eV in

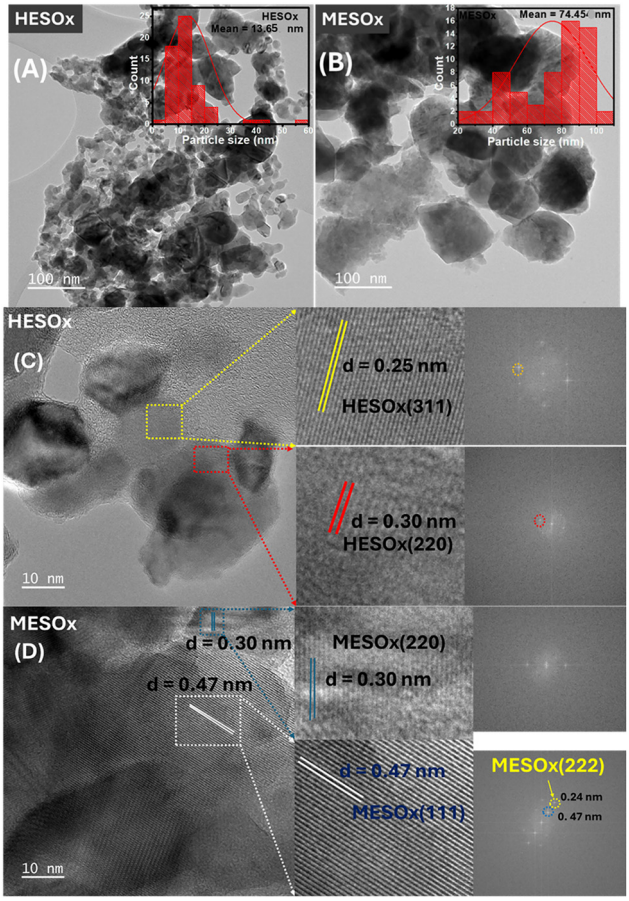


**Fig. 10** (A and B) TEM images, (C and D) HRTEM images of the samples.

the MESOx Mn 2p scan is attributed to $Mn^{2+}$, whereas another peak at 642.13 eV is attributed to $Mn^{3+}$.[71,85,97,99]

With the addition of Cu, the Co 2p and Ni 2p states of HESOx shifted to lower binding energies than MESOx, suggesting some electron transfer to Co and Ni from Cu. In contrast, the binding energies of Mn 2p and Fe 2p changed positively, suggesting electron loss in Mn and Fe.[100] In addition to the shifts, the Mn 2p of HESOx has an extra peak at 638.17 eV due to $Mn^0$, suggesting that the presence of Cu may promote reduction and the formation of Mn metal clusters or nanoparticles. The binding energies obtained from the fitting of the spectra are shown in Table 1. The Cu 2p scan of HESOx, the Cu 2p scan reveals the chemical states of Cu. The $Cu^0$ (Cu metal), $Cu^{2+}$ (CuO), and $Cu^{2+}$ ($Cu(OH)_2$) states of Cu are positioned at 932.66 eV, 933.62 eV, and 934.89 eV, respectively.

The valence band spectra (Fig. 11H & I) reveal the energy difference between the Fermi level and the valence band maximum ($E_F - E_{VBM}$), which can provide insight into the electronic structure of the transition metals of MESOx and HESOx and its impact on the electrocatalytic properties. The smaller $E_F - E_{VBM}$ value of HESOx (0.082 eV) means that its electrons are at a relatively lower energy compared to MESOx (0.209 eV), indicating a stronger interaction between the d-states of

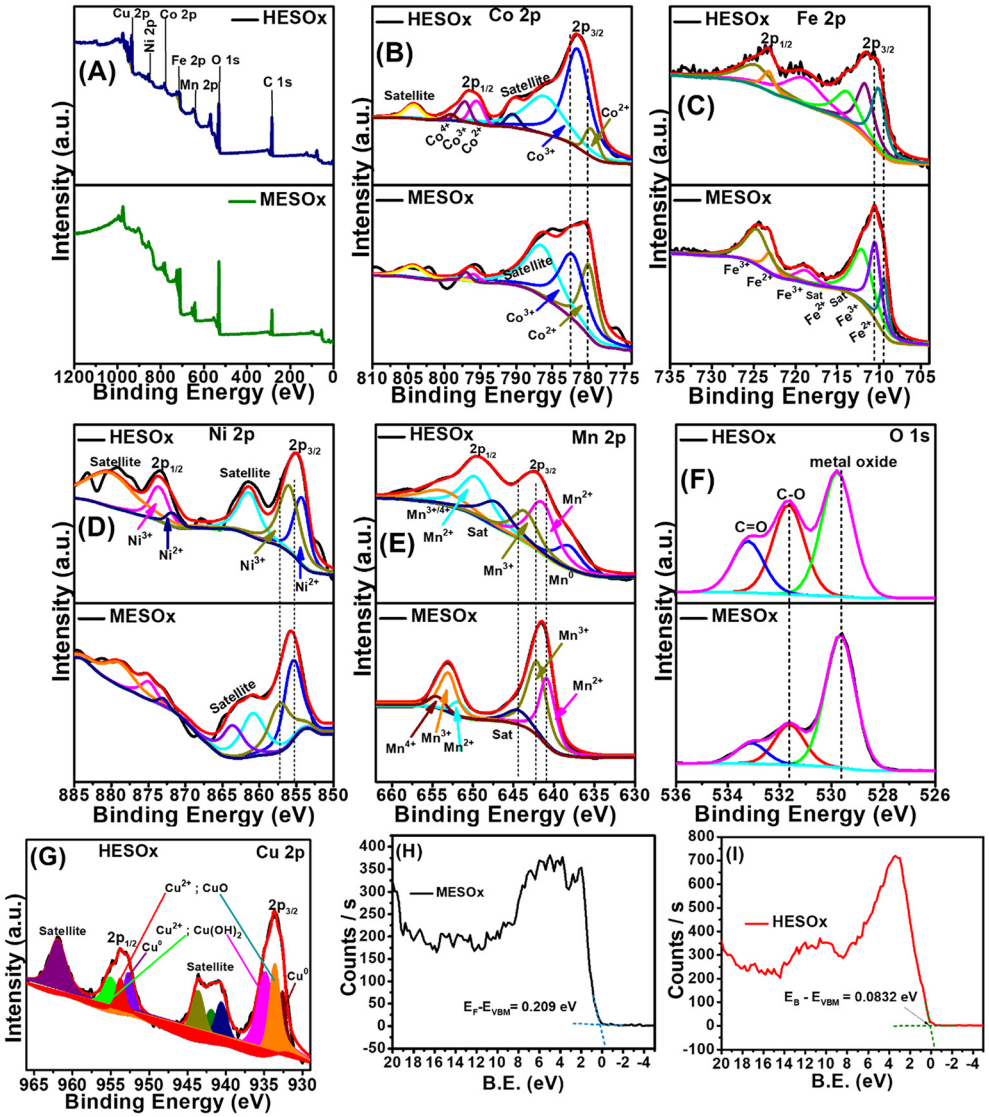


**Fig. 11** (A–G) XPS scans of MESOx and HESOx, and (H and I) their valence band spectra.

**Table 1** A summary of the XPS

| | Sample | | | | | | | |
|---|---|---|---|---|---|---|---|---|
| | Binding energies (eV)/peak area | | | | | | | |
| | HESOx | | | | MESOx | | | |
| Chemical species | $2p_{3/2}$ | Area | $2p_{1/2}$ | Area | $2p_{3/2}$ | Area | $2p_{1/2}$ | Area |
| $Cu^0$ | 932.66 | 3872.20 | 952.69 | 3613.64 | | | | |
| $Cu^{2+}$ (CuO) | 933.62 | 7654.16 | 953.76 | 2641.11 | | | | |
| $Cu^{2+}$ ($Cu(OH)_2$) | 934.89 | 11 892.69 | 955.04 | 4678.50 | | | | |
| $Ni^{2+}$ | 854.36 | 1970.87 | 871.60 | 361.99 | 855.53 | 19 702.31 | 872.80 | 878.12 |
| $Ni^{3+}$ | 855.97 | 2750.30 | 873.55 | 1216.54 | 857.27 | 15 477.81 | 874.97 | 4193.92 |
| $Co^{2+}$ | 779.53 | 7877.87 | 795.51 | 6997.12 | 779.94 | 3393.94 | 795.68 | 251.13 |
| $Co^{3+}$ | 781.53 | 42 500.06 | 797.39 | 4559.46 | 782.21 | 5208.41 | 796.97 | 165.05 |
| $Co^{4+}$ | | | 799.33 | 1212.84 | | | | |
| $Fe^{2+}$ | 710.07 | 3789.01 | 723.21 | 991.57 | 709.42 | 4397.55 | 723.05 | 2243.29 |
| $Fe^{3+}$ | 711.67 | 3818.58 | 724.75 | 2981.40 | 710.47 | 8803.41 | 724.58 | 8161.27 |
| $Mn^0$ | 638.17 | 20 126.89 | | | | | | |
| $Mn^{2+}$ | 641.45 | 47 753.11 | 649.62 | 41 365.09 | 640.76 | 3682.96 | 651.71 | 703.98 |
| $Mn^{3+}$ | 643.55 | 26 901.94 | 653.73 | 22 842.09 | 642.13 | 4979.48 | 653.12 | 2271.93 |
| $Mn^{4+}$ | | | | | | | 654.46 | 651.09 |

HESOx and its Fermi level.[75,101,102] This is in good agreement with the XPS and indicates that the presence of Cu enhances the interaction of HESOx with the reaction intermediates.

### Electrocatalytic HER performance

From the HER LSV plots of the electrocatalysts and Pt/C, which was used as the standard (Fig. 12A), the addition of Cu in the spinel mix (HESOx) results in a lower potential requirement to reach 10 mA $cm^{-2}$ (16 mV). This is lower than the overpotentials of MESOx (167 mV) and Pt/C (18 mV). The overpotentials required by each electrocatalyst to reach 10 mA $cm^{-2}$ and 100 mA $cm^{-2}$ are summarized in Fig. 12B, however, at higher overpotentials (beyond 202 mV), the performance of HESOx is observed to decline, to the reduction of cupric oxide (CuO) and hydroxide ($Cu(OH)_2$) to cuprous oxide ($Cu_2O$) in an alkaline electrolyte, thereby creating a passivating film on the surface of HESOx and blocking active sites.[152] This layer acts as a barrier to electron transfer and hinders the electrocatalytic process, giving rise to larger overpotentials at higher current densities. The Tafel slopes (Fig. 12C) calculated from LSV curves show faster HER kinetics for HESOx (106.5 mV $dec^{-1}$) than MESOx (159.5). Potentiostatic electrochemical impedance spectroscopy (PEIS) (Fig. 12D) fitted with the equivalent circuit (Fig. 12D inset) revealed a smaller solution resistance (6.12 Ω) for HESOx, compared to the resistance offered by MESOx (6.81 Ω). This lower ohmic resistance could be the primary driver for the superior initial performance of HESOx. However, HESOx reveals a slightly higher diffusion resistance ($R_{diff}$: 0.81 Ω) than MESOx (0.78 Ω), suggesting more efficient mass transport on MESOx. MESOx also displays a lower charge transfer resistance ($R_{ct}$; 657.8 Ω) compared to HESOx (749.8 Ω).

Non-faradaic CV scans were obtained at scan rates from 10 mV $s^{-1}$ to 70 mV $s^{-1}$ in steps of 10 mV $s^{-1}$ (Fig. 12E and F) and used to obtain the values of the electrical double-layer capacitance ($C_{dl}$) of HESOx and MESOx and hence the electroactive surface area (ECSA) of each sample (Fig. 12G). The higher values obtained for HESOx suggest that the addition of Cu in the entropy mix increases the active surface area, hence the higher initial catalytic performance of $(CoCuFeMnNi)_3O_4$. Using chronopotentiometry to examine the stability of HESOx under HER conditions (Fig. 12H), the potential is observed to decrease from −0.284 V to −0.246 V over 10 h.

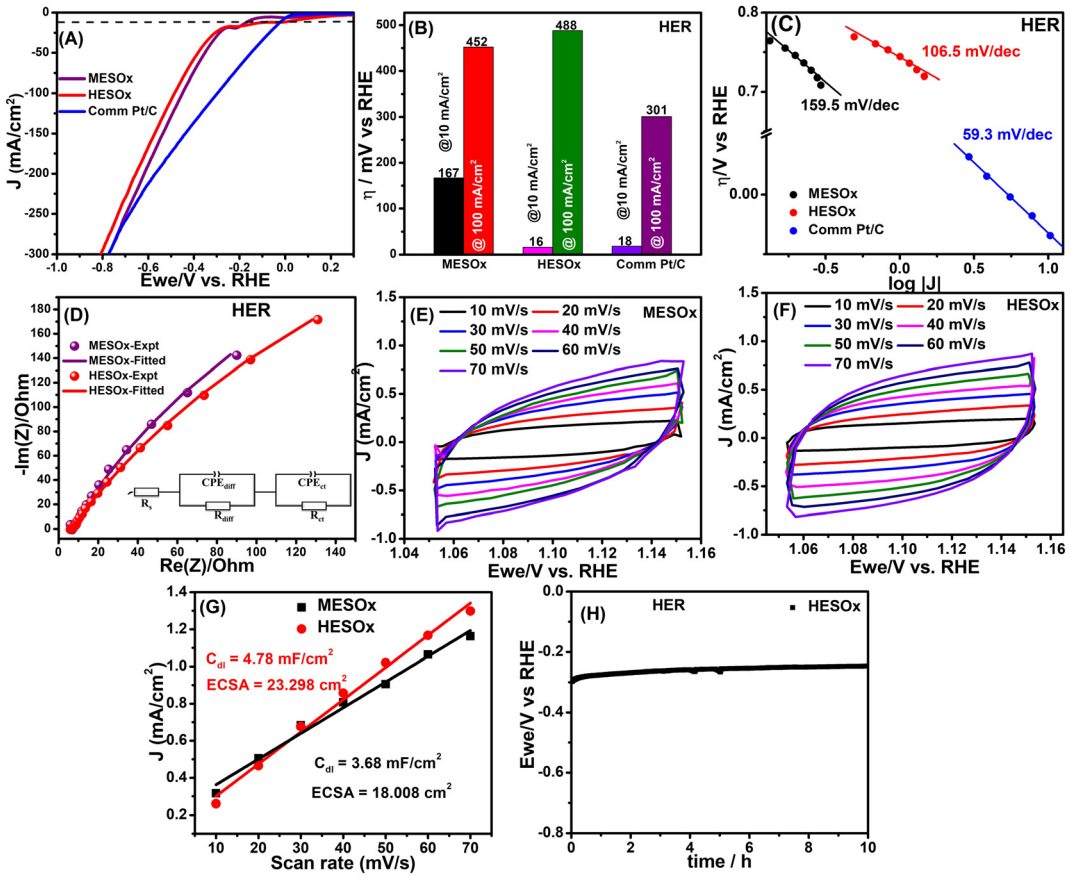


**Fig. 12** (A) HER polarization curves in 1.0 M KOH at 10 mV $s^{-1}$ and 1600 rpm, (B) HER overpotentials of the electrocatalysts at 10 mA $cm^{-2}$ and 100 mA $cm^{-2}$, (C) HER Tafel plots, (D) PEIS spectra of MESOx and HESOx (inset: equivalent circuit used in fitting the impedance spectra). (E) Non-faradaic CV scans of MESOx. (F) Non-faradaic CV scans of HESOx. (G) Plots of the current density differences *vs.* scan rates for $C_{dl}$ analysis. (H) HER chronopotentiometry test of HESOx.

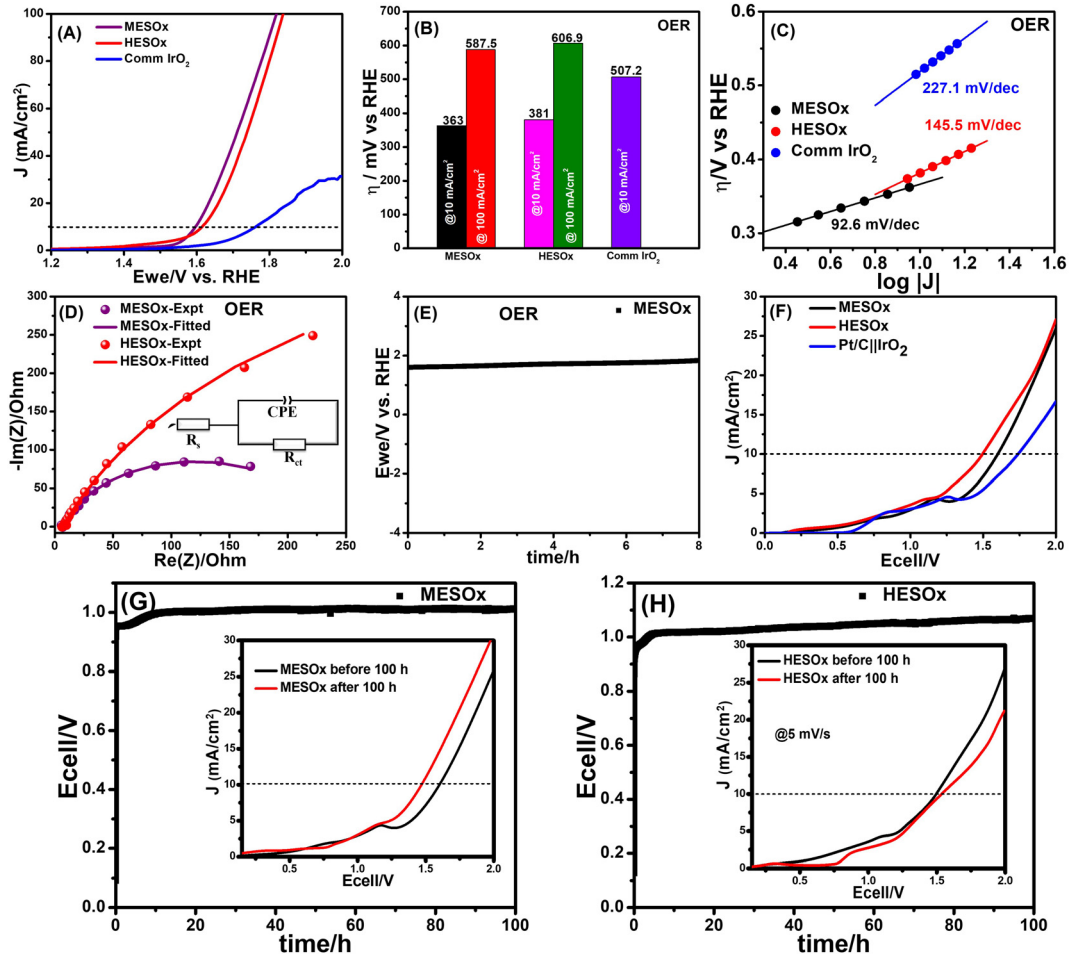


**Fig. 13** (A) OER polarization curves in 1.0 M KOH at 10 mV $s^{-1}$ and 1600 rpm. (B) OER overpotentials of the electrocatalysts at 10 mA $cm^{-2}$ and 100 mA $cm^{-2}$. (C) OER Tafel plots. (D) PEIS spectra of MESOx and HESOx. (E) OER stability test of MESOx. (F) Two-electrode water-splitting tests of MESOx, HESOx and Pt/C||$IrO_2$, and stability tests of (G) MESOx and (H) HESOx.

### Electrocatalytic OER performance

Similarly, LSV was used to evaluate the OER performances of the electrocatalysts, using $IrO_2$ as a reference. From the LSV curves in Fig. 13A, HESOx is seen to have a better performance until around 1.56 V and 5 mA $cm^{-2}$, after which it, again, gets sluggish. Hence, MESOx reaches 10 mA $cm^{-2}$ at a lower overpotential of 363 mV, lower than the overpotentials of HESOx (381 mV) and $IrO_2$ (507.2 mV). The overpotentials are summarized in Fig. 13B. The Tafel slopes (Fig. 13C) calculated from LSV curves show faster OER kinetics on MESOx. PEIS (Fig. 13D) revealed a smaller $R_{ct}$ for MESOx (228 Ω) compared to HESOx (364.8 Ω).

Chronopotentiometry was also employed to evaluate the stability of MESOx under OER conditions (Fig. 13E), and the potential increases by *ca.* 12.5% over 8 h.

### Two-electrode water-splitting test

HESOx and MESOx were evaluated for their overall water-splitting capabilities in 1 M KOH using a two-electrode setup. After dispersing 10 mg of $HESOx_{PVP\ 1\%}$ and 10 mg of OLC in 500 μL of ethanol (99.99% absolute ethanol) and 20 μL of Nafion (5 wt%) and sonicating for 30 min, the obtained catalyst ink was loaded at the anode and cathode to loading of 2 mg $cm^{-2}$ with carbon cloth (1 cm × 1 cm) as the substrate at both electrodes. LSVs obtained at 5 mV $s^{-1}$ (Fig. 13F) reveal HESOx as having the best bifunctional electrocatalytic performance, requiring a potential of ~1.50 V to reach 10 mA $cm^{-2}$, compared to the potentials of MESOx (~1.60 V) and Pt/C||$IrO_2$ (1.74 V) at 10 mA $cm^{-2}$. Under the constant current of 10 mA $cm^{-2}$ (Fig. 13G and H), MESOx is observed to be more stable than HESOx over 100 h, retaining ~94.5% of its activity, compared to the 87% activity retention of HESOx. LSV collected after 100 h shows only a slight decrease in the performance of HESOx, which requires 1.53 V to get to 10 mA $cm^{-2}$, and a tremendous improvement in the performance of MESOx, with a potential of ~1.47 V at 10 mA $cm^{-2}$, which could be attributed to the formation of new active sites.

In HESOx, the EIS data acquired before and after 100 h of operation (Fig. 14) reveal a significant decrease in $R_{ct}$ (4.772 Ω to 1.6 Ω), confirming catalyst activation and improved reaction kinetics, while the increased Warburg impedance (28.96 Ω to

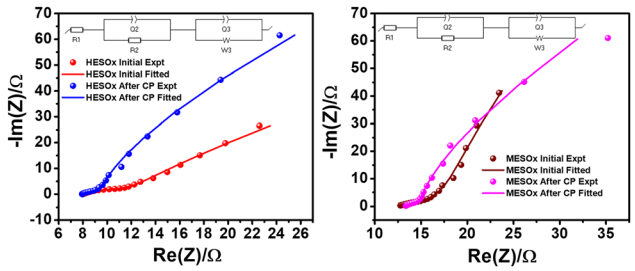


**Fig. 14** PEIS spectra of HESOx and MESOx before and after 100 h, and the equivalent circuits used in fitting them.

100.5 Ω) suggests diffusion limitations arising from continuous gas evolution during long-term water splitting. The increased post-CP LSV overpotential is therefore attributed to mass-transport limitations rather than intrinsic kinetic degradation, as evidenced by the elevated Warburg impedance, likely arising from gas bubble accumulation during the prolonged two-electrode water splitting. In contrast, MESOx shows a significant decrease in both the charge transfer resistance (7.659 Ω to 1.457 Ω) and the Warburg impedance (164.1 Ω to 112.6 Ω) after long-term chronopotentiometry, indicating improved interfacial kinetics and enhanced mass transport, resulting in lower post-CP LSV overpotentials, as seen in Fig. 13G, confirming electrochemical activation and structural robustness under continuous water-splitting conditions.

## Conclusions

A series of $(CoCuFeMnNi)_3O_4$ materials were synthesized as bifunctional electrocatalysts for alkaline water-splitting reactions *via* the reverse coprecipitation method with surfactants (CTAB, SDS, PVP) assistance at a surfactant weight percentage of 0.5%, followed by calcination. XRD shows that using surfactants in the synthesis does not alter the phase composition but influences the crystallinity of $(CoCuFeMnNi)_3O_4$. SEM and TEM observations show that PVP-assisted $(CoCuFeMnNi)_3O_4$ has a more uniform particle size distribution, while the SDS- and CTAB-assisted $(CoCuFeMnNi)_3O_4$ suffers agglomeration, probably due to an insufficient concentration of surfactants, thereby having a wide range of particle size distribution. XPS suggests more efficient catalysis on PVP-assisted $(CoCuFeMnNi)_3O_4$, and the electrochemical tests show enhanced reaction kinetics in the water-splitting reactions (HER/OER), reaching 10 mA $cm^{-2}$ at overpotentials of 87 mV and 415.8 mV, in the HER and OER, respectively. Based on the performance of the PVP-assisted $(CoCuFeMnNi)_3O_4$, different salt–PVP ratios were used to synthesize $(CoCuFeMnNi)_3O_4$, and the $(CoCuFeMnNi)_3O_4$ synthesized with 1 wt% PVP ($HESOx_{PVP\ 1\%}$) exhibits the best overall performance for HER and OER, requiring 16 mV to reach 10 mA $cm^{-2}$ in the HER and 381 mV to reach 10 mA $cm^{-2}$ in the OER. $HESOx_{PVP\ 1\%}$ is also highly efficient in the overall water-splitting bifunctionality test, achieving 10 mA $cm^{-2}$ current density at a potential of 1.497 V, and demonstrating long-term stability towards alkaline water-splitting.

MESOx was synthesized under the same conditions as HESOx ($HESOx_{PVP\ 1\%}$), and the presence of Cu in HESOx is observed to increase the specific surface area and electrochemically active surface area of the material, enhancing the initial performance of the material. However, it suffers a loss of active sites due to the possible formation of $Cu_2O$. The influence of Cu is also observed in the two-electrode test, where $(CoCuFeMnNi)_3O_4$ reaches 10 mA $cm^{-2}$ at an earlier potential of about 1.50 V compared to the 1.60 V required by $(CoFeMnNi)_3O_4$. However, after 100 h of chronopotentiometry, the performance of $(CoFeMnNi)_3O_4$ is observed to improve, requiring 1.47 V to get to 10 mA $cm^{-2}$, which is attributed to the decreased charge transfer resistance and diffusion limitations.

## Conflicts of interest

The authors declare no competing financial interests.

## Data availability

The data supporting this article have been included as part of the supplementary information (SI). Figures for the TGA, SEM, TEM, elemental analyses, XPS, XRD, Raman of the various HESOx catalysts; Electrochemical characterisation data (CV scans, ECSA); Synthesis procedures and electrode preparation processes, and several Tables detailing gas sorption and EIS data. See DOI: https://doi.org/10.1039/d5nr03192c.

## Acknowledgements

The authors are grateful to the University of the Witwatersrand (Wits), the National Research Foundation (NRF), and the Department of Science and Innovation (DSI) for financial through the DSI-NRF-Wits SARChI Chair in Materials Electrochemistry and Energy Technologies (MEET) (UID no.: 132739). J. J. Ogada thanks Wits University for supporting her doctoral degree.

## References

1 S. Trasatti, *J. Electroanal. Chem. Interfacial Electrochem.*, 1972, **39**, 163–184.
2 I. Roger, M. A. Shipman and M. D. Symes, *Nat. Rev. Chem.*, 2017, **1**, 0003.
3 Q. Liang, G. Brocks and A. Bieberle-Hütter, *JPhys Energy*, 2021, **3**, 026001.
4 Y. Jia, Y. Li, Q. Zhang, S. Yasin, X. Zheng, K. Ma, Z. Hua, J. Shi, C. Gu, Y. Dou and S. Dou, *Carbon Energy*, 2024, **6**, e528.
5 X. Wang, Y. Zheng, W. Sheng, Z. J. Xu, M. Jaroniec and S.-Z. Qiao, *Mater. Today*, 2020, **36**, 125–138.

6 B. Deng, J. Liang, L. Yue, T. Li, Q. Liu, Y. Liu, S. Gao, A. A. Alshehri, K. A. Alzahrani, Y. Luo and X. Sun, *Chin. Chem. Lett.*, 2021, **33**, 890–892.
7 C. Ye, L. Zhang, L. Yue, B. Deng, Y. Cao, Q. Liu, Y. Luo, S. Lu, B. Zheng and X. Sun, *Inorg. Chem. Front.*, 2021, **8**, 3162–3166.
8 H. Wu, Q. Huang, Y. Shi, J. Chang and S. Lu, *Nano Res.*, 2023, **16**, 9142–9157.
9 H. Qu, X. He, Y. Wang and S. Hou, *Appl. Sci.*, 2021, **11**, 4320.
10 Z. Jin, J. Lyu, Y. Zhao, H. Li, X. Lin, G. Xie, X. Liu, J.-J. Kai and H.-J. Qiu, *ACS Mater. Lett.*, 2020, **2**, 1698–1706.
11 T. Wang, H. Chen, Z. Yang, J. Liang and S. Dai, *J. Am. Chem. Soc.*, 2020, **142**, 4550–4554.
12 A. K. Ipadeola, A. K. Lebechi, L. Gaolatlhe, A. B. Haruna, M. Chitt, K. Eid, A. M. Abdullah and K. I. Ozoemena, *Electrochem. Commun.*, 2022, **136**, 107207.
13 H. Liu, H. Qin, J. Kang, L. Ma, G. Chen, Q. Huang, Z. Zhang, E. Liu, H. Lu, J. Li and N. Zhao, *Chem. Eng. J.*, 2022, **435**, 134898.
14 Z.-X. Cai, H. Goou, Y. Ito, T. Tokunaga, M. Miyauchi, H. Abe and T. Fujita, *Chem. Sci.*, 2021, **12**, 11306–11315.
15 L. Guo, Y. Huang, Y. Qin, B. Chen, C. Liu, H. Chen, J. Zhang, X. Zhang and Q. Wang, *Nanoscale*, 2025, **17**, 17312–17323.
16 T. Chen, C. Qiu, X. Zhang, H. Wang, J. Song, K. Zhang, T. Yang, Y. Zuo, Y. Yang, C. Gao, W. Xiao, Z. Jiang, Y. Wang, Y. Xiang and D. Xia, *J. Am. Chem. Soc.*, 2023, **146**, 1174–1184.
17 F. Ali, S. Mehmood, A. Ashraf, A. Saleem, U. Younas, A. Ahmad, M. P. Bhatti, G. E. Eldesoky, A. M. Aljuwayid, M. A. Habila, A. Bokhari, M. Mubashir, L. F. Chuah, W. Roy and P. L. Show, *Ind. Eng. Chem. Res.*, 2023, **62**, 4765–4777.
18 Y. Li, X. Bai, D. Yuan, C. Yu, X. San, Y. Guo, L. Zhang and J. Ye, *Nat. Commun.*, 2023, **14**, 3171.
19 Y.-H. Liu, C.-J. Hsieh, L.-C. Hsu, K.-H. Lin, Y.-C. Hsiao, C.-C. Chi, J.-T. Lin, C.-W. Chang, S.-C. Lin, C.-Y. Wu, J.-Q. Gao, C. W. Pao, Y.-M. Chang, M.-Y. Lu, S. Zhou and T. Yang, *Sci. Adv.*, 2023, **9**, eadf9931.
20 R. Akbarzadeh and H. Dehghani, *Bull. Mater. Sci.*, 2017, **40**, 1361–1369.
21 M. Mahendiran, A. Matharasi, A. AlindaShaly, G. H. Priya, J. M. Linet and T. A. Mary, *Mater. Today: Proc.*, 2022, **68**, 341–346.
22 G. Chen, J. Liu, R. Liu and Y. Li, *Ionics*, 2023, **29**, 3879–3893.
23 Y. Nakama, *Cosmet. Sci. Technol*, 2017, 231–244.
24 S. M. Morsy, *Int. J. Curr. Microbiol. Appl. Sci.*, 2014, **3**, 237–260.
25 B. E. Rapp, *Microfluidics: Modelling, Mechanics and Mathematics*, 2017, pp. 421–444.
26 R. Devivaraprasad, N. Nalajala, B. Bera and M. Neergat, *Front. Chem.*, 2019, **7**, 00648.
27 Y. Lang, X. Sun, Y. Zhang, S. Fu, S. Yan, L. Wang and G. Liang, *J. Mater. Sci.*, 2022, **57**, 4664–4683.
28 L. Jothi, R. S. Arunagirinathan and S. Mahadevan, *Mater. Lett.*, 2023, **346**, 134527.
29 J. B. Raoof, M. A. Karimi, S. R. Hosseini and S. Mangelizade, *Int. J. Hydrogen Energy*, 2011, **36**, 13281–13287.
30 Z. Zhang, Q. Liu, D. Pan, Y. Xue, X. Liu, J. Zhao, Y. Ouyang, X. Ding, S. Xiao and Q. Yang, *RSC Adv.*, 2023, **13**, 15910–15917.
31 J. Wang, C. Chen, N. Cai, M. Wang, H. Li and F. Yu, *Nanoscale*, 2021, **13**, 1354–1363.
32 X. Li, Y. Liu, J. Zhu, P. Tsiakaras and P. K. Shen, *J. Colloid Interface Sci.*, 2022, **607**, 1411–1423.
33 S. Xie, M. Yuan, T. Wang, J. Liu, J. Yan, Z. Li and J. Peng, *Ceram. Int.*, 2022, **48**, 10113–10119.
34 C. Liu, Y. Chen, L. Guo and C. Li, *Int. J. Environ. Res. Public Health*, 2018, **15**, 1654.
35 D. Wu, K. Kusada, T. Yamamoto, T. Toriyama, S. Matsumura, S. Kawaguchi, Y. Kubota and H. Kitagawa, *J. Am. Chem. Soc.*, 2020, **142**, 13833–13838.
36 Y. Yang, B. He, H. Ma, S. Yang, Z. Ren, T. Qin, F. Lu, L. Ren, Y. Zhang, T. Wang, X. Liu and L. Chen, *Acta Phys.-Chim. Sin.*, 2022, 2201050.
37 A. K. Lebechi, A. K. Ipadeola, K. Eid, A. M. Abdullah and K. I. Ozoemena, *Nanoscale*, 2022, **14**, 10717–10737.
38 E. H. Hechter, A. B. Haruna, X.-Y. Yang, M. W. Terban, H. D. Abruña, D. H. Barrett and K. I. Ozoemena, *Energy Adv.*, 2025, **4**, 1229–1240.
39 B. Talluri, K. Yoo and J. Kim, *J. Environ. Chem. Eng.*, 2022, **10**, 106932.
40 T. X. Nguyen, J. Patra, J.-K. Chang and J.-M. Ting, *J. Mater. Chem. A*, 2020, **8**, 18963–18973.
41 C. Liu, J. Bi, L. Xie, X. Gao and J. Rong, *J. Energy Storage*, 2023, **71**, 108211.
42 N. Mishra and G. Makov, *Materials*, 2022, **15**, 6015.
43 B. Issa, I. Obaidat, B. Albiss and Y. Haik, *Int. J. Mol. Sci.*, 2013, **14**, 21266–21305.
44 J. C. Navarro, C. Hurtado, M. Gonzalez-Castaño, L. F. Bobadilla, S. Ivanova, F. L. Cumbrera, M. A. Centeno and J. A. Odriozola, *J. CO2 Util.*, 2023, **68**, 102356.
45 D. Zhu, L. Wang, W. Yu and H. Xie, *Sci. Rep.*, 2018, **8**, 5282.
46 G. Panzeri, M. Cristina, M. S. Jagadeesh, G. Bussetti and L. Magagnin, *Sci. Rep.*, 2020, **10**, 18730.
47 J. Li, T. Zhao, M. M. Shirolkar, M. Li, H. Wang and H. Li, *Nanomaterials*, 2019, **9**, 790.
48 A. G. Bekru, L. D. Tufa, O. A. Zelekew, M. Goddati, J. Lee and F. K. Sabir, *ACS Omega*, 2022, **7**, 30908–30919.
49 Y. H. Hou, Y. J. Zhao, Z. W. Liu, H. Y. Yu, X. C. Zhong, W. Q. Qiu, D. C. Zeng and L. S. Wen, *J. Phys. D: Appl. Phys.*, 2010, **43**, 445003.
50 Z. Xu, H. Dong, W. Gu, Z. He, F. Jin, C. Wang, Q. You, J. Li, H. Deng, L. Liao, D. Chen, J. Yang and Z. Wu, *Angew. Chem., Int. Ed.*, 2023, **62**, e202308441.
51 J. E. Post, D. A. McKeown and P. J. Heaney, *Am. Mineral.*, 2020, **105**, 1175–1190.
52 B. Rivas-Murias and V. Salgueiriño, *J. Raman Spectrosc.*, 2017, **48**, 837–841.

53 K. Gandha, K. Elkins, N. Poudyal and J. P. Liu, *J. Appl. Phys.*, 2015, **117**, 17A736.
54 G. T.-K. Fey and D.-L. Huang, *Electrochim. Acta*, 1999, **45**, 295–314.
55 C. Vargas-Hernández, O. Almanza and J. F. Jurado, *J. Phys.: Conf. Ser.*, 2009, **167**, 12037.
56 S. Salustro, A. Erba, C. M. Zicovich-Wilson, Y. Nöel, L. Maschio and R. Dovesi, *Phys. Chem. Chem. Phys.*, 2016, **18**, 21288–21295.
57 I. O. Ali, M. S. Thabet, K. S. El-Nasser, A. M. Hassan and T. M. Salama, *Microporous Mesoporous Mater.*, 2012, **160**, 97–105.
58 A. J. P. van Zyl, D. de Wet-Roos, R. D. Sanderson and B. Klumperman, *Eur. Polym. J.*, 2004, **40**, 2717–2725.
59 J. Reiner, D. Martin, F. Ott, L. Harnisch, V. Gaukel and H. P. Karbstein, *Colloids Interfaces*, 2023, **7**, 22.
60 N. T. K. Thanh, N. Maclean and S. Mahiddine, *Chem. Rev.*, 2014, **114**, 7610–7630.
61 L. I. Atanase, in *Systems of Nanovesicular Drug Delivery*, Academic Press, 2022, pp. 17–37.
62 T. W. Hansen, A. T. DeLaRiva, S. R. Challa and A. K. Datye, *Acc. Chem. Res.*, 2013, **46**, 1720–1730.
63 E. Nazarzadeh, T. Anthonypillai and S. Sajjadi, *J. Colloid Interface Sci.*, 2013, **397**, 154–162.
64 S. T. Gentry, S. F. Kendra and M. W. Bezpalko, *J. Phys. Chem. C*, 2011, **115**, 12736–12741.
65 J. J. Ogada, A. K. Ipadeola, P. V. Mwonga, A. B. Haruna, F. Nichols, S. Chen, H. A. Miller, M. V. Pagliaro, F. Vizza, J. R. Varcoe, D. M. Meira, D. M. Wamwangi and K. I. Ozoemena, *ACS Catal.*, 2022, **12**, 7014–7029.
66 T. J. Ehirim, O. C. Ozoemena, P. V. Mwonga, A. B. Haruna, T. P. Mofokeng, K. De Wael and K. I. Ozoemena, *ACS Omega*, 2022, **7**, 47892–47905.
67 H. Chen, N. Qiu, B. Wu, Z. Yang, S. Sun and Y. Wang, *RSC Adv.*, 2020, **10**, 9736–9744.
68 C. A. Corlett, N. Obradovic, J. L. Watts, E. W. Bohannan and W. G. Fahrenholtz, *J. Asian Ceram. Soc.*, 2023, **11**, 330–337.
69 J. J. Ogada, T. J. Ehirim, A. K. Ipadeola, A. B. Haruna, P. V. Mwonga, A. M. Abdullah, X.-Y. Yang, K. Eid, D. M. Wamwangi and K. I. Ozoemena, *ACS Omega*, 2024, **9**, 7439–7451.
70 Y. Ito, M. Izumi, D. Hojo, M. Wakisaka, T. Aida and T. Adschiri, *Chem. Lett.*, 2017, **46**, 267–270.
71 S. Bhowmick, M. K. Mohanta and M. Qureshi, *Sustainable Energy Fuels*, 2021, **5**, 6392–6405.
72 H. Xia, D. Zhu, Z. Luo, Y. Yu, X. Shi, G. Yuan and J. Xie, *Sci. Rep.*, 2013, **3**, 2978.
73 A. Shekhawat, R. Samanta and S. Barman, *ACS Appl. Energy Mater.*, 2022, **5**, 6059–6069.
74 Q. Ai, Z. Yuan, R. Huang, C. Yang, G. Jiang, J. Xiong, Z. D. Huang and S. Yuan, *J. Mater. Sci.*, 2018, **54**, 4212–4224.
75 E. Gioria, S. Li, A. Mazheika, R. Naumann d'Alnoncourt, A. Thomas and F. Rosowski, *Angew. Chem., Int. Ed.*, 2023, **26**, e202217888.
76 A. K. Kar and R. Srivastava, *Inorg. Chem. Front.*, 2019, **6**, 576–589.
77 T. Soe, A. Jityen, T. Kongkaew, K. Subannajui, A. Sinsarp and T. Osotchan, *AIP Conf. Proc.*, 2020, **2279**, 140002.
78 X. Chen, D.-H. Kuo, A. D. Saragih, Z.-Y. Wu, H. Abdullah and J. Lin, *Chem. Eng. Sci.*, 2019, **194**, 105–115.
79 D. C. Kaseman, A. G. Jarvi, X. Y. Gan, S. Saxena and J. E. Millstone, *Chem. Mater.*, 2018, **30**, 7313–7321.
80 M. El, A. M. Elbanna, G. E. Khedr and N. K. Allam, *Energy Adv.*, 2023, **2**, 2129–2139.
81 J. Chen, W. Huang, S. Bao, W. Zhang, T. Liang, S. Zheng, L. Yi, L. Guo and X. Wu, *RSC Adv.*, 2022, **12**, 27746–27765.
82 X. Wang, B. Zhang, W. Zhang, M. Yu, L. Cui, X. Cao and J. Liu, *Sci. Rep.*, 2017, **7**, 1584.
83 B. Li, X. Yuan, B. Li and X. Wang, *Fuel*, 2021, **301**, 121027.
84 G. S. Dhillon, G. Cao and N. Yi, *Catalysts*, 2023, **13**, 1171.
85 J. Wang, M. Zhang, F. Li, H. Wang, Y. Chen and H. Song, *New J. Chem.*, 2022, **46**, 22672–22685.
86 M. B. Islam, M. Yanagida, Y. Shirai, Y. Nabetani and K. Miyano, *ACS Omega*, 2017, **2**, 2291–2299.
87 H. Rong, T. Chen, R. Shi, Y. Zhang and Z. Wang, *ACS Omega*, 2018, **3**, 5634–5642.
88 H. Zhang, T. Wang, A. Sumboja, W. Zang, J. Xie, D. Gao, S. J. Pennycook, Z. Liu, C. Guan and J. Wang, *Adv. Funct. Mater.*, 2018, **28**, 1804846.
89 J. X. Flores-Lasluisa, J. Quílez-Bermejo, A. C. Ramírez-Pérez, F. Huerta, D. Cazorla-Amorós and E. Morallón, *Materials*, 2019, **12**, 1302.
90 D. Yin, J. Tang, R. Bai, S. Yin, M. Jiang, Z. Kan, H. Li, F. Wang and C. Li, *Nanoscale Res. Lett.*, 2021, 16.
91 T. Yamashita and P. Hayes, *Appl. Surf. Sci.*, 2008, **254**, 2441–2449.
92 X. Lu, X. Chen, W. Zhou, Y. Tong and G.-R. Li, *ACS Appl. Mater. Interfaces*, 2015, **7**, 14843–14850.
93 Y. Yan, H. Tang, F. Wu, R. Wang and M. Pan, *Energies*, 2017, **10**, 1296.
94 C. Elmi, S. Guggenheim and R. Gieré, *Clays Clay Miner.*, 2016, **64**, 537–551.
95 A. Ramírez, P. Hillebrand, D. Stellmach, M. M. May, P. Bogdanoff and S. Fiechter, *J. Phys. Chem. C*, 2014, **118**, 14073–14081.
96 T. Liu, X. Ma, D. Liu, S. Hao, G. Du, Y. Ma, A. M. Asiri, X. Sun and L. Chen, *ACS Catal.*, 2016, **7**, 98–102.
97 P. Plate, C. Höhn, U. Bloeck, P. Bogdanoff, S. Fiechter, F. F. Abdi, R. van de Krol and A. C. Bronneberg, *ACS Appl. Mater. Interfaces*, 2021, **13**, 2428–2436.
98 K. Natarajan, M. Saraf and S. M. Mobin, *Nanoscale*, 2018, **10**, 13250–13260.
99 S. Chen, H. Huang, P. Jiang, K. Yang, J. Diao, S. Gong, S. Liu, M. Huang, H. Wang and Q. Chen, *ACS Catal.*, 2019, **10**, 1152–1160.
100 R. He, L. Yang, Y. Zhang, X. Wang, S. Lee, T. Zhang, L. Li, Z. Liang, J. Chen, J. Li, A. O. Moghaddam, J. Llorca, M. Ibanez, J. Arbiol, Y. Xu and A. Cabot, *Energy Storage Mater.*, 2023, **58**, 287–298.

 

101 Z. Zhang, B. Li, Q. Qian, X. Tang, M. Hua, B. Huang and K. J. Chen, *IEEE Trans. Electron Devices*, 2017, **64**, 4036–4043.
102 N. Kalita, U. Nath, A. Singha, M. Sarma and M. Qureshi, *J. Mater. Chem. A*, 2025, **13**, 10723–10735.
103 Y. Zheng, X. Wu, X. Lan and R. Hu, *Processes*, 2021, **10**, 49.
104 A. Kumar, N. Kumar and Y. Sharma, *Ionics*, 2018, **25**, 707–718.
105 P. Mukherjee, K. Sathiyan, R. S. Vishwanath and T. Zidki, *Mater. Chem. Front.*, 2022, **6**, 1770–1778.
106 T. Kwon, M. Jun, G. J. Bang, H. Yang, J. Joo, T. Kim, J. Kim, J. M. Kim, H. Baik, Y. Jung, J. Y. Kim and K. Lee, *Cell Rep. Phys. Sci.*, 2020, **1**, 100260.
107 C. C. L. McCrory, S. Jung, J. C. Peters and T. F. Jaramillo, *J. Am. Chem. Soc.*, 2013, **135**, 16977–16987.
108 M. Sadaqat, S. Manzoor, L. Nisar, A. Hassan, D. Tyagi, J. H. Shah, M. N. Ashiq, K. S. Joya, T. Alshahrani and M. Najam-ul-Haq, *Electrochim. Acta*, 2021, **371**, 137830.
109 A. Roy, K.-M. Kang, Y.-C. Nah, M. La, D. Choi and S. J. Park, *Electrochim. Acta*, 2021, **383**, 138368.
110 M. R. Gennero de Chialvo and A. C. Chialvo, *J. Electrochem. Soc.*, 2000, **147**, 1619.
111 J. Durst, A. Siebel, C. Simon, F. Hasché, J. Herranz and H. A. Gasteiger, *Energy Environ. Sci.*, 2014, **7**, 2255–2260.
112 F. Bao, E. Kemppainen, I. Dorbandt, R. Bors, F. Xi, R. Schlatmann, R. Krol and S. Calnan, *ChemElectroChem*, 2021, **8**, 195–208.
113 T. Shinagawa, A. T. Garcia-Esparza and K. Takanabe, *Sci. Rep.*, 2015, **5**, 13801.
114 J. Zheng, W. Sheng, Z. Zhuang, B. Xu and Y. Yan, *Sci. Adv.*, 2016, **2**, e1501602.
115 N. Mahmood, Y. Yao, J.-W. Zhang, L. Pan, X. Zhang and J.-J. Zou, *Adv. Sci.*, 2017, **5**, 1700464.
116 D. Pan, Q. Liu, B. Yu, D. B. DuBois, J. Tressel, S. Yu, N. Kaleekal, S. Trabanino, Y. Jeon, F. Bridges and S. Chen, *Small*, 2024, **20**, 202404729.
117 A. Wu, Y. Xie, V. C. Li, C. Tian, Y. Gu, H. Yan, X. Zhang, G.-Y. Yang and H. Fu, *Nano Energy*, 2018, **44**, 353–363.
118 Y. Wang, H. Arandiyan, S. S. Mofarah, X. Shen, S. A. Bartlett, P. Koshy, C. C. Sorrell, H. Sun, C. Pozo-Gonzalo, K. Dastafkan, S. Britto, S. K. Bhargava and C. Zhao, *Adv. Mater.*, 2024, **36**, 2402156.
119 Q. Mo, Y. Meng, L. Qin, C. Shi, H.-B. Zhang, X. Yu, J. Rong, P.-X. Hou, C. Liu, H.-M. Cheng and J.-C. Li, *ACS Appl. Mater. Interfaces*, 2024, **16**, 16164–16174.
120 P. Muthukumar, M. Pannipara, A. G. Al-Sehemi, D. Moon and S. P. Anthony, *New J. Chem.*, 2022, **46**, 12558–12564.
121 C. Duan, X. Li, D. Wang, Z. Wang, H. Sun, R. Zheng and Y. Liu, *Sustainable Energy Fuels*, 2022, **6**, 1479–1488.
122 B. Feng, J. Chen, Y. Yang, M. Yang, H. Wang, C. Zhong, X. Zhao and Y. Yao, *J. Materiomics*, 2024, **10**, 919–927.
123 C. Kim, S. Lee, S. H. Kim, I. Kwon, J. Park, S. Kim, J. Lee, Y. S. Park and Y. Kim, *Nanoscale Adv.*, 2021, **3**, 6386–6394.
124 T. Priamushko, P. Guggenberger, A. Mautner, J. Lee, R. Ryoo and F. Kleitz, *ACS Appl. Energy Mater.*, 2022, **5**, 13385–13397.
125 V. Do, P. Prabhu, V. Jose, T. Yoshida, Y. Zhou, H. Miwa, T. Kaneko, T. Uruga, Y. Iwasawa and J. Lee, *Adv. Mater.*, 2023, **35**, 202208860.
126 X. Xu, H. Liang, G. Tang, Y. Hong, Y. Xie, Z. Qi, B. Xu and Z. Wang, *Nanoscale Adv.*, 2019, **1**, 177–183.
127 K. R. Park, J. E. Jeon, G. Ali, Y.-H. Ko, J. Lee, H. Han and S. Mhin, *Catalysts*, 2019, **9**, 564.
128 X.-S. Gong, X. Liu and J. Zhou, *Nanoscale*, 2025, **17**, 5301–5315.
129 S. C. Pathan, J. S. Shaikh, N. S. Shaikh, V. Márquez, M. Rittiruam, T. Saelee, P. Khajondetchairit, S. S. Mali, J. V. Patil, C. K. Hong, P. Praserthdam and S. Praserthdam, *S. Afr. J. Chem. Eng.*, 2024, **48**, 425–435.
130 Y. Wang, J. Xiao, T. Huang, Y. Wang, H. Ding, Q. Zhu, G. Xu and L. Zhang, *Nanoscale*, 2025, **17**, 14278–14289.
131 Z. Guo, Y. He, P. Chen, R. Li, Z. Wang, X. Xu, S. Chang, Y. Li, R. Jia and S. Han, *Int. J. Hydrogen Energy*, 2024, **92**, 1500–1507.
132 B. Zhang, X. Qian, H. Xu, L. Jiang, J. Xia, H. Chen and G. He, *Nanoscale*, 2023, **15**, 16199–16208.
133 Sk. Riyajuddin, T. Aziz, S. Kumar, G. D. Nessim and K. Ghosh, *ChemCatChem*, 2020, **12**, 1394–1402.
134 S. Ahmad, M. Egilmez, W. Abuzaid, F. Mustafa, A. M. Kannan and A. S. Alnaser, *Int. J. Hydrogen Energy*, 2024, **52**, 1428–1439.
135 C.-L. Huang, Y.-G. Lin, C.-L. Chiang, C.-K. Peng, D. S. Raja, C.-T. Hsieh, Y.-A. Chen, S.-Q. Chang, Y.-X. Yeh and S.-Y. Lu, *Appl. Catal., B*, 2023, **320**, 122016.
136 S. Wang, B. Xu, W. Huo, H. Feng, X. Zhou, F. Fang, Z. Xie, J. K. Shang and J. Jiang, *Appl. Catal., B*, 2022, **313**, 121472.
137 T. Song, L. Zhang, P. Zhang, J. Zeng, T. Wang, A. Ali and H. Zeng, *J. Mater. Chem. A*, 2017, **5**, 6013–6018.
138 R. Nivetha, A. Sajeev, A. M. Paul, K. Gothandapani, S. Gnanasekar, P. Bhardwaj, G. Jacob, R. Sellappan, V. Raghavan, N. K. Chandar, S. Pitchaimuthu, S. K. Jeong and A. N. Grace, *Mater. Res. Express*, 2020, **7**, 114001.
139 B. N. Khiarak, M. Mojaddami, Z. Z. Faradonbeh, A. O. Zekiy and A. Simchi, *Energy Fuels*, 2022, **36**, 4502–4509.
140 K. Kannimuthu, K. Sangeetha, S. S. Sankar, A. Karmakar, R. Madhu and S. Kundu, *Inorg. Chem. Front.*, 2021, **8**, 234–272.
141 J.-B. Raoof, S. R. Hosseini, R. Ojani and S. Mandegarzad, *Energy*, 2015, **90**, 1075–1081.
142 A. Roy, D. Hursán, K. Artyushkova, P. Atanassov, C. Janáky and A. Serov, *Appl. Catal., B*, 2018, **232**, 512–520.
143 A. S. Sabir, E. Pervaiz, R. Khosa and U. Sohail, *RSC Adv.*, 2023, **13**, 4963–4993.
144 O. A. Restrepo, Ó. Arnache and N. Mousseau, *Materialia*, 2024, **33**, 102031.
145 Q. Chen, T. Gao, L. Chen, B. Miao and Q. Chen, *Ceram. Int.*, 2024, **50**, 26234–26249.
146 R. T. Parayil, S. K. Gupta, K. Garg, S. Mehta, K. Sudarshan, M. Mohapatra and T. C. Nagaiah, *Sustainable Energy Fuels*, 2024, **8**, 2144–2152.

147 J. Ruiz-Fuertes, T. Bernert, M. He, B. Winkler, V. L. Vinograd and V. Milman, *Appl. Phys. Lett.*, 2014, **105**, 071911.
148 M.-K. Ho, Y.-T. Yu, H.-H. Chiu, K. Manjunatha, S.-L. Yu, B.-L. Lyu, T.-E. Hsu, H.-C. Kuo, S.-W. Yu, W.-C. Tu, C.-Y. Chang, C.-L. Cheng, H. Nagabhushana, T.-T. Lin, Y.-R. Hsu, M.-C. Chen, Y.-L. Huang and S. Y. Wu, *Nanomaterials*, 2025, **15**, 1093.
149 Z. A. Alothman, *Materials*, 2012, **5**, 2874–2902.
150 K. A. Cychosz and M. Thommes, *Engineering*, 2018, **4**, 559–566.
151 M. Thommes, K. Kaneko, A. V. Neimark, J. P. Olivier, F. Rodriguez-Reinoso, J. Rouquerol and K. S. W. Sing, *Pure Appl. Chem.*, 2015, **87**, 1051–1069.
152 M. Zhou, C. Lian, Z. Xu, T. Pi, K. Yang, B. Chi and Z. Li, *Appl. Surf. Sci.*, 2020, **505**, 144653.

 